THESIS

PALEO-FEEDBACKS IN THE HYDROLOGICAL AND ENERGY CYCLES IN THE COMMUNITY CLIMATE SYSTEM MODEL 3

Submitted by

Melissa A. Burt

Department of Atmospheric Science

COLORADO STATE UNIVERSITY

April 29, 2008

WE HEREBY RECOMMEND THAT THE THESIS PREPARED UNDER OUR SUPERVISION BY MELISSA A. BURT ENTITLED PALEO-FEEDBACKS IN THE HYDROLOGICAL AND ENERGY CYCLES IN THE COMMUNITY CLIMATE SYSTEM MODEL 3 BE ACCEPTED AS FULFILLING IN PART REQUIREMENTS FOR THE DEGREE OF MASTER OF SCIENCE.

Committee on Graduate work

_____

_____

_____

_____

_____
Adviser

_____
Department Head

ABSTRACT OF THESIS

PALEO FEEDBACKS IN THE HYDROLOGICAL AND ENERGY CYCLES IN THE
COMMUNITY CLIMATE SYSTEM MODEL 3

The hydrological and energy cycles are examined using the Community Climate System Model version 3 (CCSM3) for two climates, the Last Glacial Maximum (LGM) and Present Day. CCSM3, developed at the National Center for Atmospheric Research, is a coupled global climate model that simulates the atmosphere, ocean, sea ice, and land surface interactions.

The Last Glacial Maximum occurred 21 ka (21,000 yrs before present) and was the cold extreme of the last glacial period with maximum extent of ice in the Northern Hemisphere. During this period, external forcings (i.e. solar variations, greenhouse gases, etc.) were significantly different in comparison to present. The "Present Day" simulation discussed in this study uses forcings appropriate for conditions before industrialization (Pre-Industrial 1750 A.D.).

This research focuses on the joint variability of the hydrological and energy cycles for the atmosphere and lower boundary and climate feedbacks associated with these changes at the Last Glacial Maximum.

The LGM simulated climate experiences a global cooling of 4.9 K compared to the PI climate, with greatest cooling in the high latitudes of both hemispheres.

Additional cooling also exists over the continental ice sheets in North America, Northern Europe, and Antarctica. Precipitation and evaporation are reduced by 10%, and precipitable water by 20%, compared to conditions at PI. Overall, from LGM to PI the changes in clouds are weak.

The water vapor, ice-albedo, and cloud feedbacks act to amplify the climate change from LGM to PI. The positive water vapor and ice-albedo feedbacks account for $5.04 \text{ W m}^{-2} \text{ K}^{-1}$ and $2.38 \text{ W m}^{-2} \text{ K}^{-1}$, respectively of the climate change. The cloud feedbacks produces -2.83 of the change. An interesting and unexpected result was that the sign of the ice-albedo feedback changed regionally and is driven by changes in ocean basin size. Combined, the radiative feedbacks from LGM to PI act to amplify the climate change by $5.67 \text{ W m}^{-2} \text{ K}^{-1}$ and are balanced by an increase in surface evaporation.

Melissa A. Burt
Department of Atmospheric Science
Colorado State University
Fort Collins, CO 80523
Summer 2008

ACKNOWLEDGEMENTS

TABLE OF CONTENTS

LIST OF TABLES

LIST OF FIGURES

CHAPTER 1

Introduction

Last Glacial Maximum (LGM), defined as the climate at about 21 ka (21000 years BP), was the peak of the last glacial period, when large inland ice sheets reached their maximum extent. Two of the largest ice sheets during the LGM were in the Northern Hemisphere, the Laurentide and Fennoscandian ice sheets, located over North America and Northern Europe, respectively. Figure 1.1 is a map produced by the Climate/Long-Range Investigation Mapping and Prediction (CLIMAP) of the Northern Hemisphere ice sheets at Last Glacial Maximum. During the Last Glacial Maximum, sea ice areas were approximately 11.5 million km^2 and 33.7 million km^2 in the Northern and Southern Hemispheres, respectively.

Understanding how climate has changed in the past can help us to gain a better idea of how climate may change in the future. Proxy records have been used in the development of reconstructions of the climate of the Last Glacial Maximum and other periods. The use of proxy records and the progress of paleoclimate modeling since the

1970s has helped us to examine and understand the climate of these periods. See Chapter

2, Section 2.3 for a brief history of progress in paleoclimate modeling.
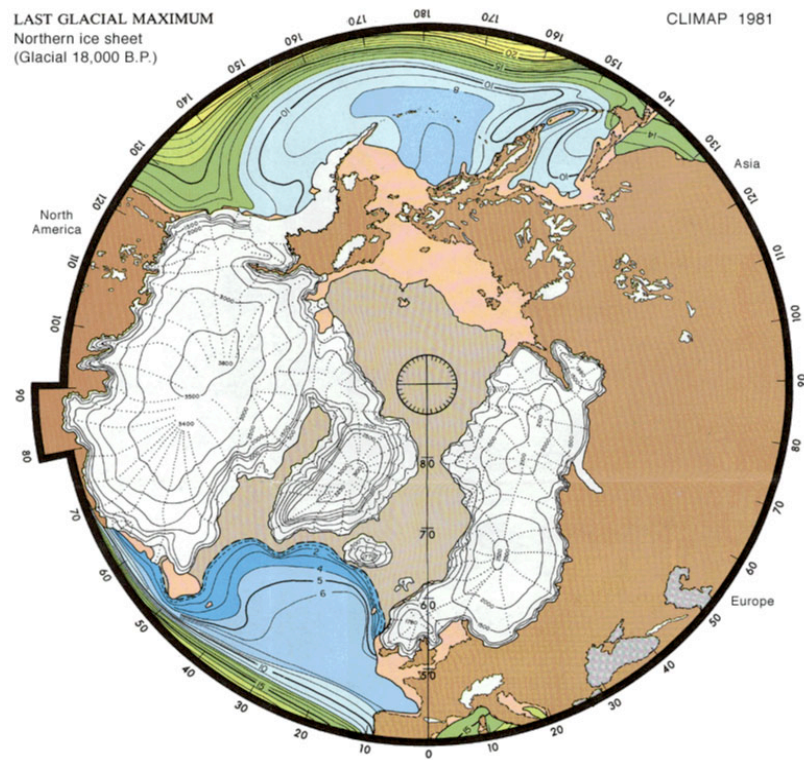
Figure 1.1: Map produced by Climate/Long-Range Investigation Mapping and Prediction (CLIMAP) of the Northern Hemisphere ice sheets at Last Glacial Maximum (CLIMAP 1981)

In this study we examine the climate feedbacks that have occurred since the Last

Glacial Maximum, using a Paleoclimate Modeling Intercomparison Project (PMIP-2)

simulation of the Community Climate System Model (CCSM3) developed at the National

Center for Atmospheric Research. The simulated Last Glacial Maximum climate is

compared with the simulated Pre-Industrial climate, the period before industrialization,

nominally at about 1800 A.D. Previous work using the LGM PMIP-2 simulation was

performed by Otto-Bliesner et al. (2006a), in which the climate sensitivity of CCSM3

was studied for two past climates, namely the LGM and Mid-Holocene. The Holocene is

the current interglacial period, which began approximately 10 ka (10000 years BP). The

simulated mean climates were examined and results were compared with proxy records and previous simulations. As an example, sea ice extent can be inferred from foraminifera paleotemperatures. CCSM3 was in good agreement with the proxies for LGM sea ice extent, although winter extent was overestimated in some regions. From the work of Otto-Bliesner et al. (2006), this particular LGM CCSM3 simulation has done a reasonably good job of representing the LGM climate.

Most model simulations that evaluate climate change feedbacks are for future scenarios. Since we do not have data for the future, it is hard to determine how well the models represent the climate. With paleoclimate simulations, proxy records exist and can be used to compare how well the model represents the climate. Because Otto-Bliesner et al. (2006a) has already compared results to proxies and we know that CCSM3 has done a reasonable good job simulating the climate; we can now analyze the climate change feedbacks.

The objectives of this study are to (1) compare the simulated hydrological and energy cycle changes between the Last Glacial Maximum and Pre-Industrial, (2) assess how these cycles interact, (3) analyze the climate feedbacks that occur due to these cycle changes, and (4) determine if the feedbacks act to amplify the climate change between LGM and PI. It is our hope that the results of this study will contribute to further advancements in understanding the climate at the Last Glacial Maximum and other past climates, and also provide a better understanding of future climate change.

The global hydrological cycle is an integral part of the Earth's climate system and is closely coupled to the global energy cycle. Together, the energy and water cycles play a strong role in determining the large-scale atmospheric circulation and precipitation

(Peixoto and Oort 1992). Within the climate system, water can be found in three phases: gas, liquid, and solid. As water evaporates from the oceans and land surface, it is then transported as water vapor by the atmosphere. See Figure 1.2. Clouds are produced and water precipitates out onto the ocean and land surfaces. This cycle incorporates the net atmospheric transport of water from the ocean to the land and then its return through the flow (in rivers) of freshwater from the land back into the oceans. Clouds are composed of water in the liquid and frozen phases and play a dominant role in maintaining the energy budget (Peixoto and Oort 1992).
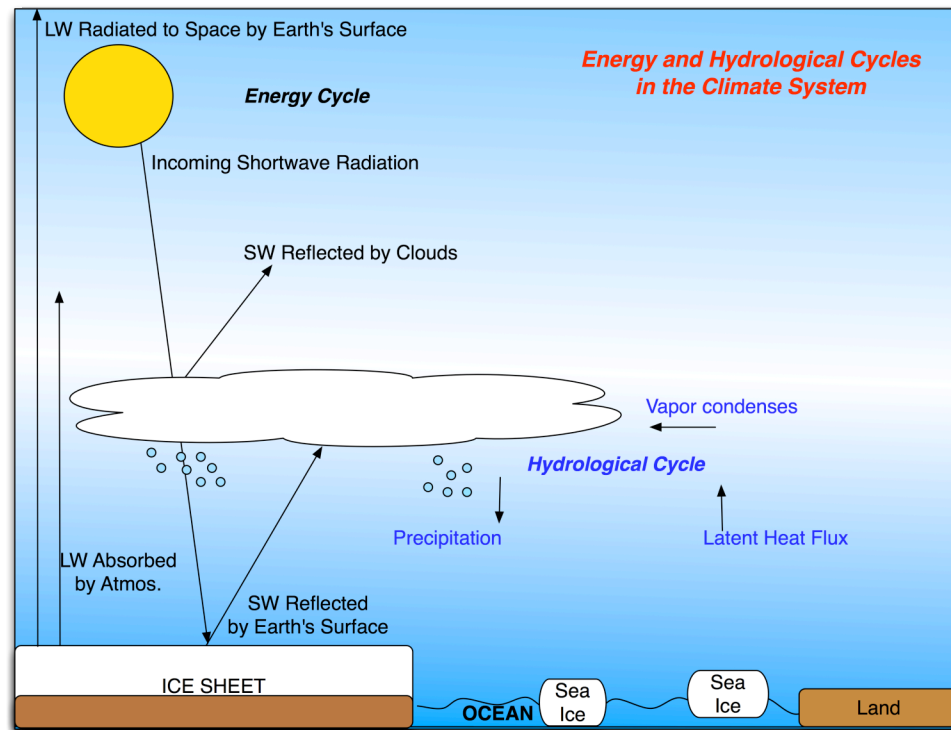
Figure 1.2: Schematic of how the hydrological and energy cycles affect the climate system.

Clouds act to cool the Earth by reflecting shortwave (solar) radiation to space and warm the Earth's surface by absorbing longwave (infrared) radiation emitted by the Earth surface, which contributes to the greenhouse effect. A cloud feedback occurs due to

changes in these cloud effects. Cloud feedbacks can arise from changes in the cloud amount, top height, and cloud optical properties. Changes in the climate during an ice age or global warming include changes in the distribution of clouds. The resulting cloud feedbacks can either amplify or damp changes in the globally averaged surface temperature. Further discussion of cloud and other radiative feedbacks is given in Chapter 3.

The glacial climate and orbital theory are discussed in Chapter 2. An overview of climate feedbacks is given in Chapter 3. Chapter 4 outlines the experimental design and methods. Mean climate results and an analysis of feedbacks as a result of the mean climate are discussed in Chapters 5 and 6, respectively. Concluding remarks and thoughts about future work follow in Chapter 7.

CHAPTER 2

Glacial Climate

2.1 Last Glacial Period

The last glacial period began approximately 116,000 years ago (116 ka), and the peak of this glacial period is known as the Last Glacial Maximum (LGM), defined as the climate at about 21 ka and extended until 14 ka. Deglaciation occurred approximately from 14 ka to 10 ka and the current interglacial, the Holocene, is from about 10 ka to 0 ka (Crowley and North 1991).

2.2 Orbital Theory

The climate system undergoes strong seasonal variations due to the movement of Earth around the Sun in its orbit. The seasonal and latitudinal distribution of solar radiation at the top of the atmosphere (i.e., insolation) is modified by periodic changes of the Earth's orbit around the sun. The Earth's orbit is elliptical, and the departure of the orbit from circularity is known as the orbital eccentricity. The eccentricity of the Earth's orbit varies between 0.002 and 0.050, with periodicities of around 100,000 and 400,000 years (Jansen et al. 2007).

Precession is the change in direction or wobble of the Earth's axis of rotation

relative to the fixed stars. Precession of the equinoxes and solstices

modulate the seasonal cycle of insolation and the position of the seasons in the orbit.

This occurs with periodicities of about 19,000 and 23,000 years. The obliquity of the

Earth's axis (i.e., axial tilt) changes with a periodicity of around 41,000 years, varies

between 22.05º and 24.50º, and has an impact on seasonal contrasts. Obliquity also

modulates insolation changes annually at low and high latitudes. It should be noted that

globally averaged, there is no change in insolation due to obliquity (Jansen et al. 2007).

Changes in the eccentricity, precession, and obliquity of the Earth's orbit (see Figure 2.1)

alter the amount and location of solar radiation reaching the Earth's surface, and can

ultimately result in 100,000-year glacial-interglacial cycles.
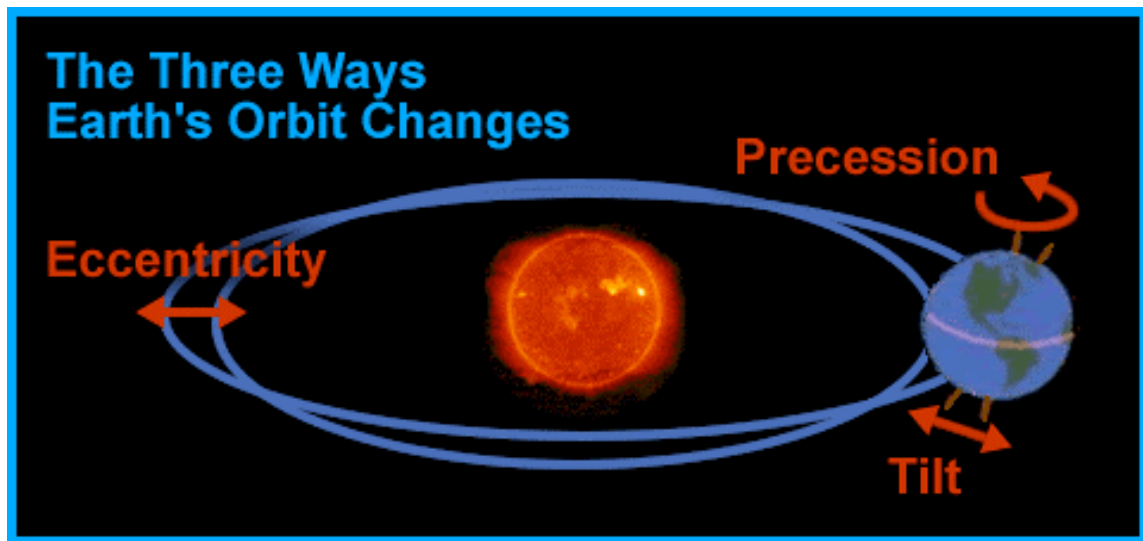
Figure 2.1: Changes in eccentricity, precession, and obliquity are ways in which the Earth's orbit changes. Adapted from Windows to the Universe (UCAR 2008).

2.2.1 Milankovitch Theory

In the early twentieth century as a theoretician and professor at the University of Belgrade, Milutin Milankovitch, decided that he would develop mathematical theory to describe the climate of Earth, Mars, and Venus at present and the past. He dubbed this a journey into "distant worlds and times" (Imbrie and Imbrie 1979). His objectives were to (1) describe the geometry of each planet's orbit and to show how the orbits have evolved, (2) calculate how much solar radiation reaches the Earth's surface during each season at a particular latitude, and (3) calculate radiation curves for latitudes in the Northern Hemisphere. These three objectives were completed by 1930, twenty years after introducing the ideas to his colleagues.

While completing these three objectives, Milankovitch determined that modulations in the Earth's obliquity, precession, and eccentricity play an important role in the glacial cycles of the Earth. He calculated the slow changes in the Earth's orbit by measurements of the position of the stars, and through equations using the gravitational pull of other planets (Imbrie and Imbrie 1979). Milankovitch made note that the earth wobbles in its orbit and the tilt of the Earth causes seasons, and as the tilt of the Earth's axis changes, the strength of the seasons also changes.

Milankovitch published, in 1920, in his *Mathematical Theory of Heat Phenomena Produced by Solar Radiation*, formulas that described the intensity of incoming solar radiation as a function of latitude and season. He stated that the same calculations could be done for past climates and argued that changes in radiation were enough to cause ice ages. In 1924, he sent one of his radiation curves to Wladamir Köppen, a German climatologist, who later published Milankovitch's radiation curve for 65ºN, which

identified four European Ice Ages and the minima of summer insolation associated with each (Figure 2.2). The final version of Milankovitch's astronomical theory of the ice ages was published in 1938. He attributed the onset of ice ages to a minimum in summer insolation at high latitudes (roughly 65° N), which is due to variations in the obliquity and precession. Such a minimum enables winter snowfall to persist all year and accumulate to build the northern hemisphere ice sheets.
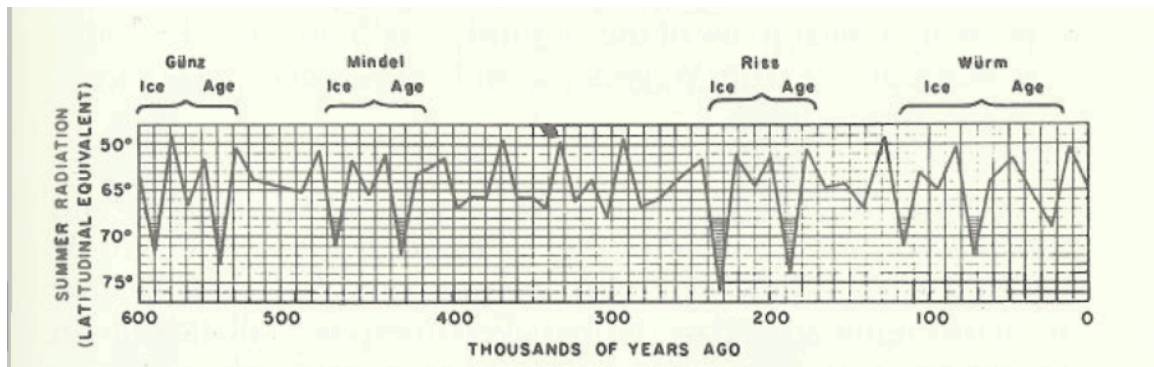
Figure 2.2: Milankovitch radiation curve for 65° North latitude published in 1924. This figure identifies four European Ice Ages and the minima of summer insolation (June-July-August) associated with these Ice Ages. Adapted from Imbrie and Imbrie (1997).

Table 2.1 shows the differences in eccentricity, obliquity, and angular precession between the Last Glacial Maximum and Pre-Industrial. Differences in eccentricity, obliquity, and angular precession are small when it comes to forcings for the LGM climate.

Table 2.1: Differences in eccentricity, obliquity and angular precession between the LGM (21 ka) and Pre-Industrial (0 ka). There are slight differences in these variables, which indicates that these are not the most important forcings for the LGM climate. Orbital parameters for 1950 A.D. are used for 0 ka (Braconnot et al. 2007).

	Eccentricity	Obliquity (degrees)	Angular precession (degrees)
0 ka	0.017	23.45	102.04
21 ka	0.019	22.95	114.42

Figure 2.3, adapted from the Intergovernmental Panel on Climate Change Fourth

Assessment Report (IPCC AR4; Jansen et al. 2007), indicates similar results to what

Milankovitch argued. The bottom right panel of Figure 2.3 is the June-July-August (JJA)

irradiance deviations with respect to present of the latitudinal distribution of solar

radiation. Minima in insolation are found roughly at 65ºN, around 116 ka. This was

approximately the onset of the last glacial period, corresponding to an insolation

40 W m^{-2} lower than present in JJA.
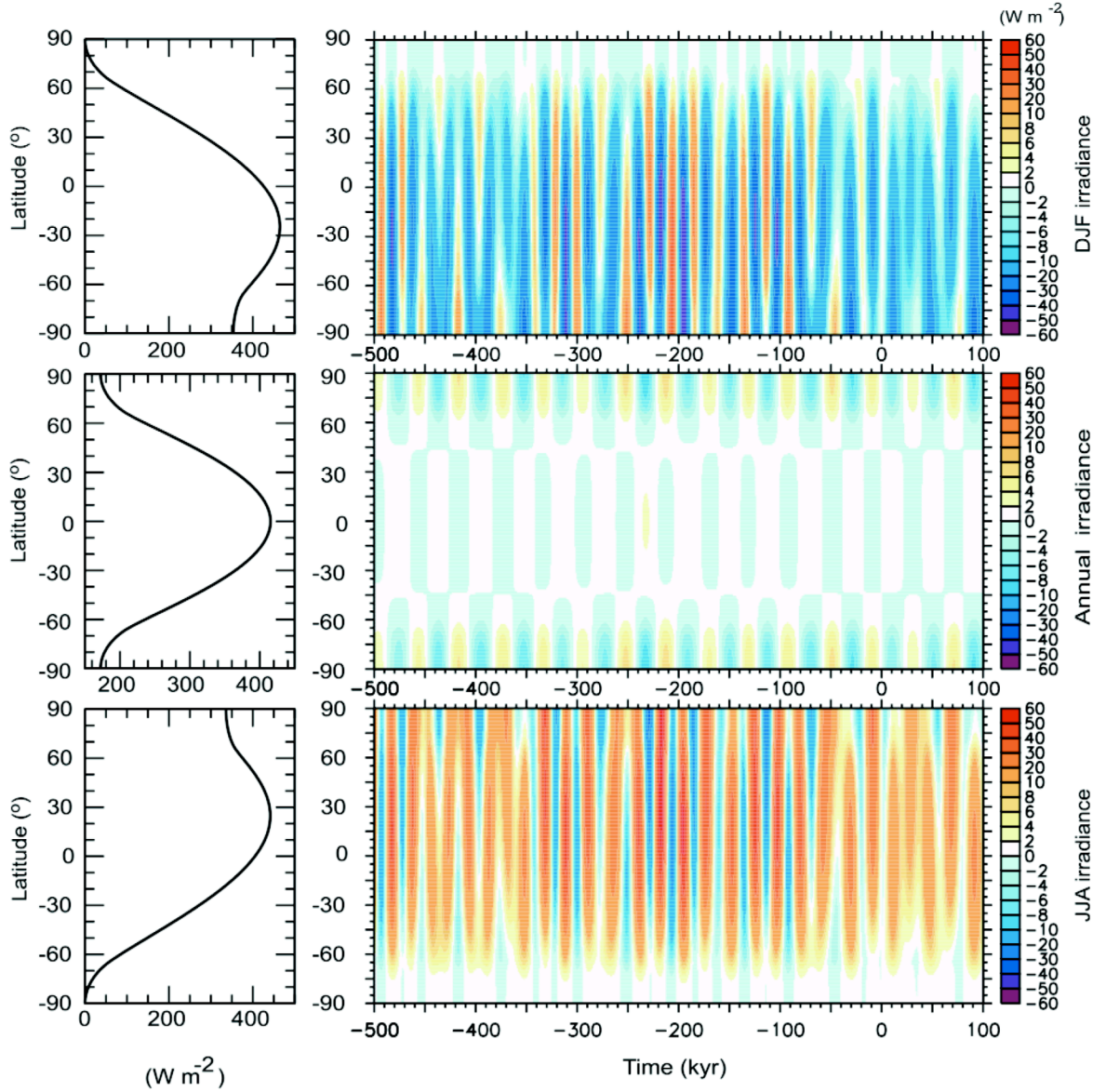
Figure 2.3: On the left hand side of the figure, December, January, February (DJF), annual mean, and June, July, August (JJA) latitudinal distribution of incoming solar radiation (W m^{-2}) at present in the top, middle, and bottom panels respectively. On the right hand side of the figure, deviations with respect to present for DJF, Annual, and JJA latitudinal distribution of incoming solar radiation (W m^{-2}). Time is in kyr (1000 yr before present). Adapted from Jansen et al. 2007.

2.3 Last Glacial Maximum

At the Last Glacial Maximum, inland ice sheets reached their maximum extent, and the ice areas in the Northern and Southern Hemisphere were approximately 11.5 and 33.7 million km^2, respectively (Bracconet et al. 2007). Much of this area is presently ice-free. The most impressive entities at the LGM were these massive inland ice sheets that encompassed both hemispheres. The largest accumulation of ice cover in the Northern Hemisphere was in Eastern North America, and made up the Laurentide Ice sheet, which connected with the Cordilleran Ice sheet at the Continental Divide. The Laurentide Ice Sheet stretched from the Rocky Mountains eastward to the Atlantic Shore, and from the Arctic Ocean to the present positions of the Ohio and Missouri Rivers (Crowley and North, 1991).

In Northwestern Europe, the greatest ice accumulation was the Fennoscandian ice sheet, which extended from Northern Germany to the Netherlands. The Laurentide and Fennoscandian ice sheets had an estimated ice thickness on the order of 3500 and 1200 meters respectively. Reductions in sea level of 120 m at LGM exposed land in many areas and caused the Bering Strait to close, which cutoff heat transport from the North Pacific to the Arctic, resulting in colder Arctic temperatures.

2.3.1 Paleoclimate Modeling efforts

An effort to study climates of the past, in particular the LGM, began in the 1970's with the Climate/Long-Range Investigation, Mapping, and Prediction (CLIMAP). CLIMAP's pioneering efforts, focused on reconstructing the climate conditions during the LGM from sediment cores and by radiocarbon age dating. The result was to produce seasonal maps of ice sheets, sea surface temperatures, and vegetation. (See Figure 1.1).

Most of the LGM modeling efforts after CLIMAP used one of the following two approaches: prescribing global observed or reconstructed sea surface temperatures (Gates 1976, Manabe and Hahn 1977, and Kutzbach and Wright 1985); or prescribing oceanic heat transport with a mixed layer ocean to mimic the effect of the ocean circulation (Hewitt and Mitchell, 1997, and Broccoli, 2000). The Paleoclimate Modeling Intercomparison Project (PMIP) was launched in 1992 to evaluate climate models under paleoclimate conditions of the Last Glacial Maximum and Holocene, and to improve the understanding of past climate change. The second phase of PMIP (PMIP-2, 2003) is conducting a modeling intercomparison study using ocean-atmosphere (OAGCM) and ocean-atmosphere-vegetation (OAVGCM) global climate model simulations, to assess the ability to simulate the LGM and Holocene and to determine the role of climate feedbacks that arise in the climate system. PMIP scientists analyzed model-model and model-data comparisons in hopes of providing benchmarks for models being used in future climate change projections.

CHAPTER 3

Feedbacks in the Climate System

The Earth's climate system is very complex and evolves due to both internal and external processes. These external processes or forcings, whether natural (e.g., volcanic eruptions) or anthropogenic (e.g., changes in atmospheric trace gases), act to change the climate system. External forcings are not affected by changes in the climate system.

The atmosphere, hydrosphere, cryosphere, biosphere, and land surface are the major components of the climate system. These components are connected through fluxes of momentum, energy, and mass. Changes within one subsystem may provoke changes throughout the rest of the climate system. The interactions and exchanges that occur between the various components can act to amplify or damp the climate response, and are referred to as climate feedbacks. Interactions that amplify the response are positive feedbacks, whereas the interactions that damp the response are negative feedbacks (Bradley 1999). Feedbacks are internal processes within the climate system, and interact with each other to amplify or damp the response to changes in external forcing.

Since this study uses a global climate model simulation, it is important to distinguish between nature and the model. As discussed earlier, feedbacks occur due to changes in forcings. Table 3.1 shows the differences between forcings and feedbacks within the climate system (i.e., nature) and global climate models. Sea level, for example, is prescribed in models and is therefore a forcing. As the models are improved, model forcings eventually become feedbacks, as they are in nature. It should be noted that some important feedbacks (e.g., aerosols, vegetation, and biogeochemical feedbacks) are not incorporated in most global climate model simulations.

Table 3.1: Differences between forcings and feedbacks within the climate system (i.e., nature) and global climate models.

	Nature	Models
Orbital changes	Forcing	Forcing
Greenhouse Gases	Feedback	Forcing
Ice Sheets	Feedback	Forcing
Sea Level	Feedback	Forcing
Vegetation changes	Feedback	Not Included
Aerosol changes	Feedback	Not Included
Water vapor feedback	Feedback	Feedback
Lapse rate feedback	Feedback	Feedback
Ice-Albedo feedback	Feedback	Feedback
Cloud feedback	Feedback	Feedback
Biogeochemical feedback	Feedback	Not Included

Suppose that there has been an external perturbation (e.g., a change in atmospheric greenhouse gases), which is imposed on the climate system (Figure 3.1). This external forcing leads to changes in the Earth's radiation budget. The climate system responds to this radiative imbalance by changing its global mean temperature (e.g., Randall et al., 2007). Changes in the global mean temperature can lead to further

warming of the climate system. Together the initial external pertubation and further changes to the climate system yield a feedback loop, which can be positive or negative.

I will give an overview of the radiative feedbacks that interact with the climate system and are associated with the Earth's radiation budget. For each feedback a figure is used to show how it works. The feedback begins once external changes occur in the climate system. The feedback then acts to amplify (positive sign) or damp (negative sign) the initial change. A positive (negative) sign indicates a positive (negative) feedback, as in Figure 3.1.
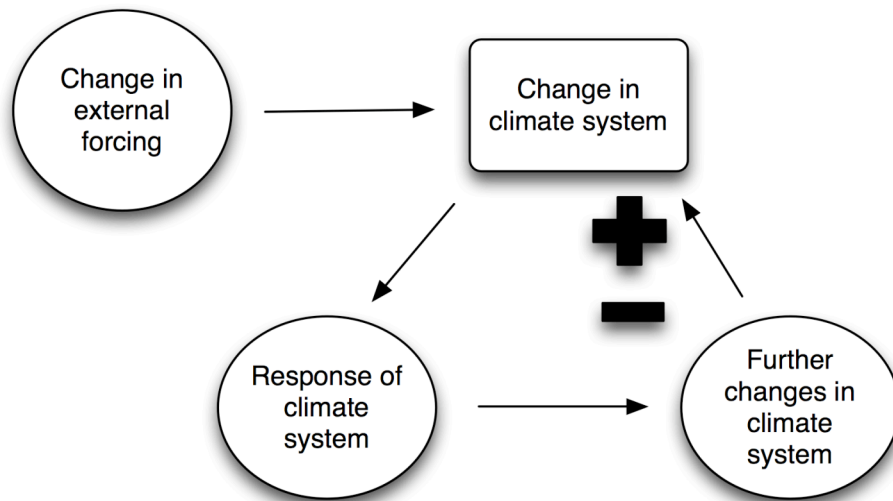
Figure 3.1: Schematic of an external forcing leading to a climate response.

Water vapor feedback:

The change in the radiative effects of water vapor due to a change in the external forcing of the climate is known as the water vapor feedback. Water vapor is one of the most important greenhouse gases and an efficient absorber of longwave radiation. Changes in the amount or vertical distribution of water vapor can change the Earth's ability to radiate heat to space. An increase in water vapor content will increase the

greenhouse effect of the atmosphere and raise the Earth's temperature (e.g., Randall et al. 2007). From the Clausius-Clapeyron relation, which describes the relationship between temperature and saturation vapor pressure (i.e., water vapor), the maximum amount of water vapor air can hold increases rapidly with temperature. The increase of water vapor with temperature constitutes one of the strongest positive feedbacks in the climate system and acts to amplify the effect of other feedbacks in the system. As illustrated in Figure 3.2, as greenhouse gases increase, tropospheric temperatures increase, leading to more atmospheric water vapor and an enhanced greenhouse effect. These changes result in a positive water vapor feedback. It should be noted that as water vapor increases, precipitation and evaporation also increase.
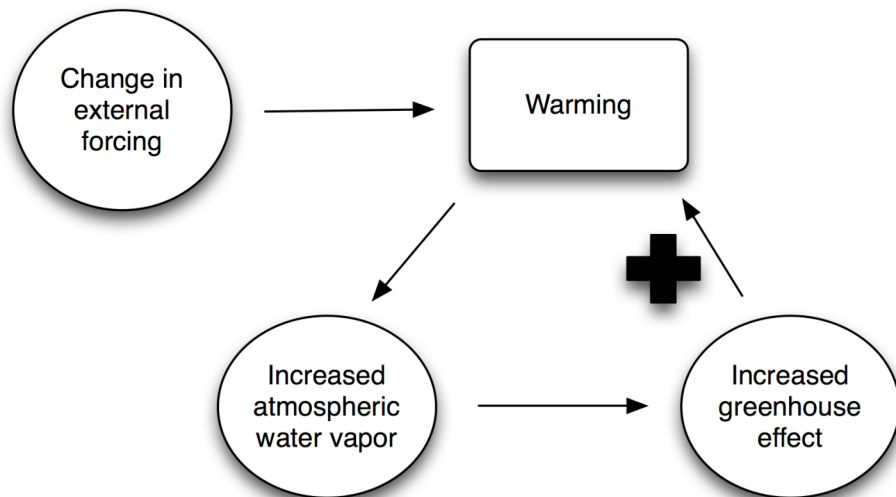
Figure 3.2: Schematic of the water vapor feedback.

Ice-albedo feedback:

A strong relationship exists between the amount of the Earth's surface covered by snow/ice and the surface albedo, ratio of the reflected shortwave and incoming solar radiation. Decreases in snow and ice cover lead to a reduced surface albedo. Ice cover

has a much higher albedo than all other surfaces and the annual variations of surface

albedo are controlled mostly by changes in snow and ice cover. The albedo of sea ice is

roughly 60%, whereas the surrounding ocean albedo is approximately 10%. These

differences have a significant impact on the Earth's radiation budget (Hartmann, 1994).

As depicted in Figure 3.3, as greenhouse gases rise, surface temperatures warm, which

leads to increased melting of snow and ice. Due to this melting, there is increased

absorption of solar radiation and reduced surface albedo. This further reinforces

warming and therefore is a positive feedback.
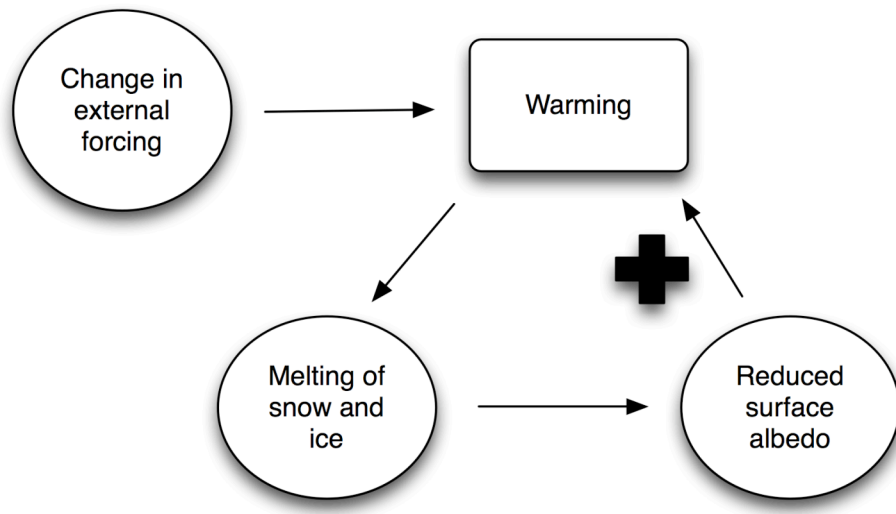
Figure 3.3: Schematic of the ice-albedo feedback.

Lapse rate feedback:

The rate at which temperature decreases with height is the lapse rate. The lapse

rate in the troposphere affects the atmospheric emission of longwave radiation to space.

Large-scale dynamical, radiative, and convective processes determine the tropospheric

lapse rate. The radiative processes act to increase the lapse rate, thereby cooling the

atmosphere and heating the surface. The convective and dynamical processes decrease the lapse rate and move heat upward in the atmosphere (Bony et al. 2006).

The lapse rate feedback is typically negative for the Earth as a whole. In the tropics, under global warming scenarios, there is a larger tropospheric warming at higher altitudes than at the surface. The tropical lapse rate is close to the moist adiabatic lapse rate, which decreases as surface temperatures increase, leading to a negative lapse rate feedback. The moist adiabatic lapse rate is the rate at which saturated air parcels cool with altitude as they are raised adiabatically. In middle and high latitudes, there is more warming at the surface than at higher altitudes, yielding a positive lapse rate feedback (Bony et al. 2006). On average, the low latitude negative lapse rate feedback dominates over the positive lapse rate feedback of the extratropics. As the climate warms, there will be temperature changes throughout the troposphere with greater warming aloft than at the surface, resulting in a decreased moist adiabatic lapse rate. See Figure 3.4.
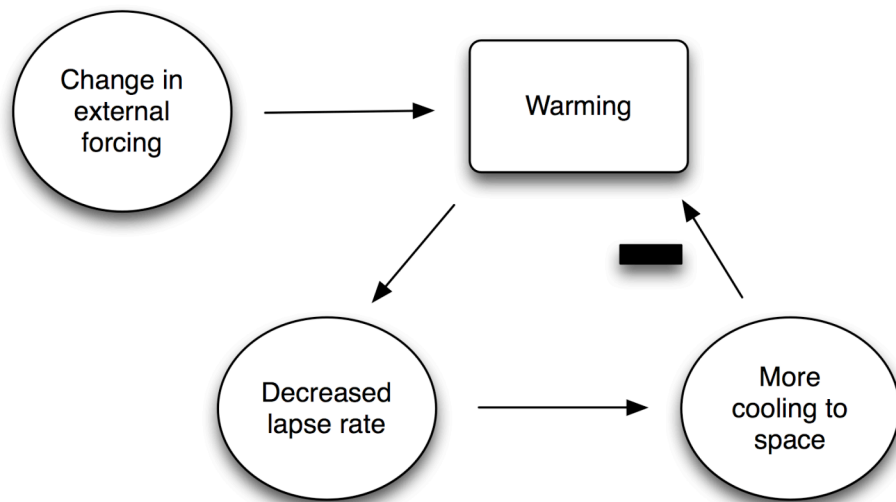
Figure 3.4: Schematic of the lapse rate feedback.

Cloud feedback:

As water vapor condenses to form clouds, the clouds can have either a cooling or a warming effect. Low, thick clouds reflect shortwave and cool the surface of the Earth, whereas high, thin clouds transmit incoming shortwave radiation and trap some of the outgoing longwave radiation (OLR) emitted by Earth. The energy is then radiated downward, warming the surface of the Earth. The balance between the warming and cooling of clouds is close, but cooling dominates and has a strong impact on the Earth's radiation budget (Hartman 1994).

The cloud feedback is dependent on cloud amount, cloud top height, and the optical properties of the cloud, and can be a positive or negative feedback. Examples of cloud feedbacks due to changes in low and high clouds are illustrated in Figures 3.5 and 3.6.
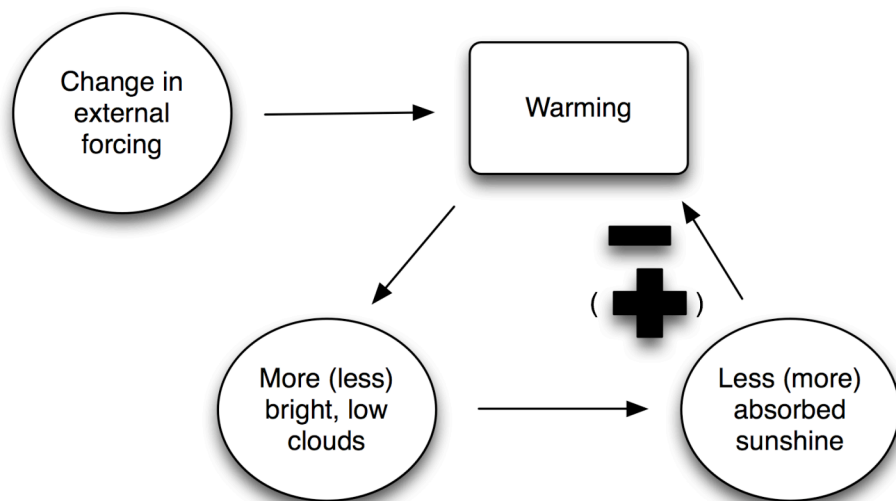
Figure 3.5: Schematic of the low cloud feedback.
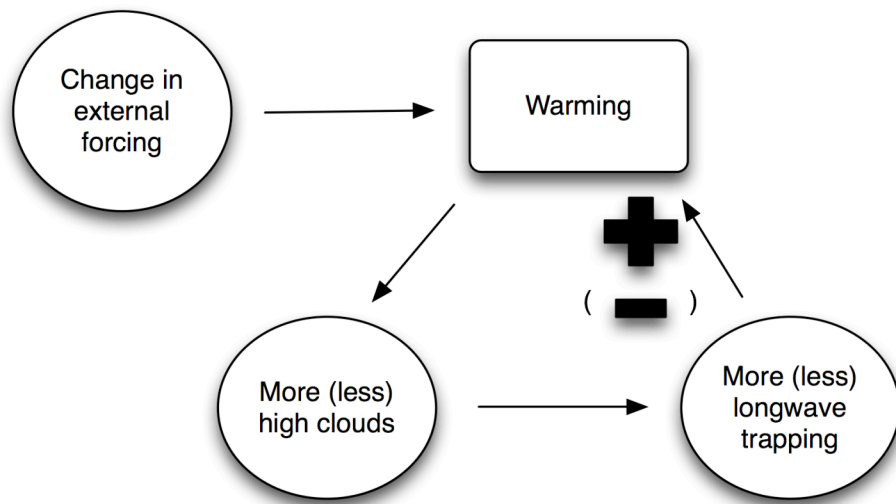
Figure 3.6: Schematic of the high cloud feedback.

Biogeochemical feedback:

This feedback is very important, but is currently not incorporated in most global climate models. As greenhouse gases increase, a warming occurs and the exchange of carbon between the atmosphere and carbon reservoirs in the ocean and land may be altered (National Research Council 2003). Changes in temperature can affect carbon stored by frozen soils (i.e., permafrost), the ocean, and the uptake of carbon by plants. These potential feedbacks can alter the carbon dioxide and methane concentrations in the atmosphere. They are believed to be positive feedbacks (Figure 3.7).
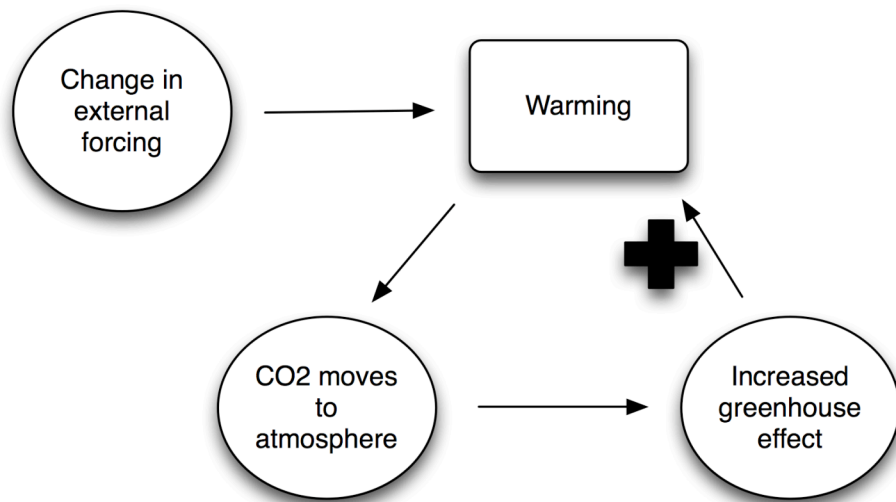
Figure 3.7: Schematic of biogeochemical feedback.

3.1 Climate Feedbacks in Global Climate Models

Various climate feedbacks (e.g., water vapor, clouds, surface albedo, and lapse rate) can interact with each other and lead to an even greater positive or negative feedback. Figure 3.8 (Bony et al. 2006), indicates the strength of each of these feedbacks within global climate models used in the IPCC AR4, and also indicates the amount of uncertainty associated with the feedback type. The water vapor feedback is the strongest positive feedback, as indicated in the far left column, whereas the lapse rate feedback has the greatest negative feedback. The global mean temperature response is amplified by the water vapor feedback and reduced by the lapse rate feedback. Cloud feedbacks have the greatest uncertainty, and can act to amplify the temperature response by 10-50%, depending on the model. Overall, the combined effect of the feedback parameters is to increase the warming by a factor of 2. This means that the feedbacks are very important.
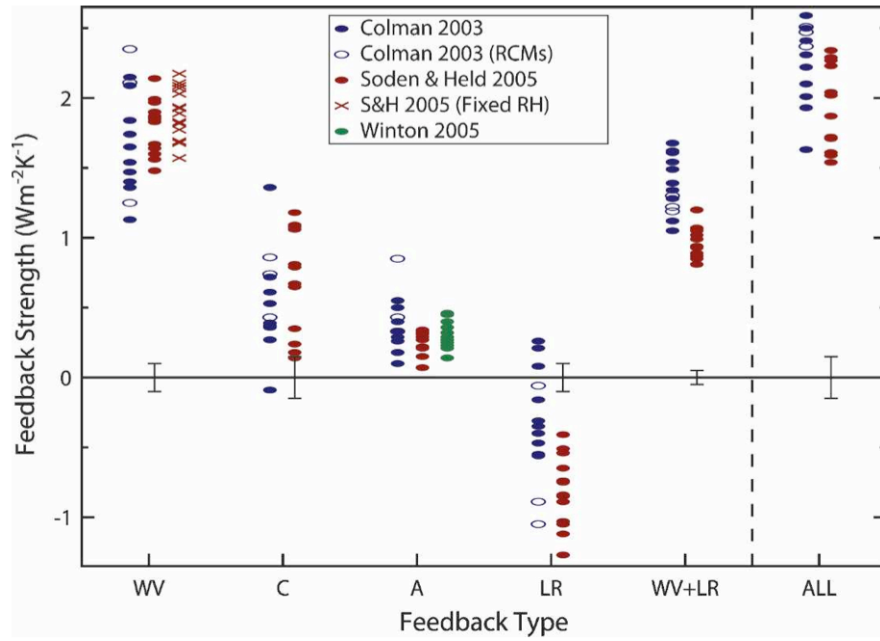
Figure 3.8: Feedback parameter strength comparisons in global climate models used in the IPCC AR4. From (left to right) is the water vapor (WV), cloud (C), albedo (A), lapse rate (LR), water vapor plus lapse rate (WV + LR), and the combined effect of each feedback (ALL). The error bars represent the amount of uncertainity with each feedback (Bony et al. 2006).

CHAPTER 4

Model Description and Experimental Design

4.1   CCSM History

The Climate System Model (CSM1), developed at the National Center for

Atmospheric Research (NCAR) in 1996, was a fully coupled model that included an

atmosphere, land surface, ocean, and sea ice components. A 300-year simulation was run

with the first version of the CSM. In 1998, the second version of CSM was released to

improve the efficiency of computing software and correct the air-sea drag coefficient

from the initial 300-year simulation (Blackmon et al. 2001). In 2000, the third release of

the CSM improved the physics in all of the component models. The CSM was renamed

the Community Climate System Model (CCSM) because of the involvement of the

climate modeling community. New land and sea ice components were implemented as

well as a new base code for the ocean. These changes were made partially because

CCSM runs on a parallel computer whereas CSM did not (Kiehl and Gent 2004). A brief

description of the physics in and experiments done with the earlier versions of CCSM can

be found in Table 4.1.

Table 4.1: Versions of the Community Climate System Model. Adapted from Blackmon et al. (2001).

Date	Version	Physics and experiments
May 1996	CSM 1.0	*Journal of Climate,* Jun 1998 (Vol. 11, No. 6); 300-yr control for 1996 conditions; 130-yr 1% per year CO_2 increase
Jun 1998	CSM 1.3	Corrected air–ice drag coefficient; prognostic liquid water formulation; many atmospheric gases included in radiative transfer parameterization; 270-yr control for 1870 conditions (Boville et al. 2001); 3 twentieth century simulations; 5 twenty-first century simulations
Jun 1999	PaleoCSM	T31 CCM3 and ×3 ocean model; ocean anisotropic horizontal viscosity, and enhanced resolution at the equator; 200-yr control for 1980 conditions; 50-yr run for conditions of the last glacial maximum; 100-yr run for mid-Cretaceous conditions
Jan 2002	CCSM-2	Improved components and coupler

The Community Climate System Model Version 3 (CCSM3), released 23 June 2004, and developed at NCAR, is a coupled global climate model that simulates the atmosphere, ocean, sea ice, and land surface interactions (Figure 4.1). The component models of CCSM3 are linked through a coupler in which fluxes and state information are exchanged. A brief discussion of the model components follows. A full model description of CCSM3 can be found in the *Journal of Climate* Special Issue on the Community Climate System Model introduced by (Collins et al. 2006).
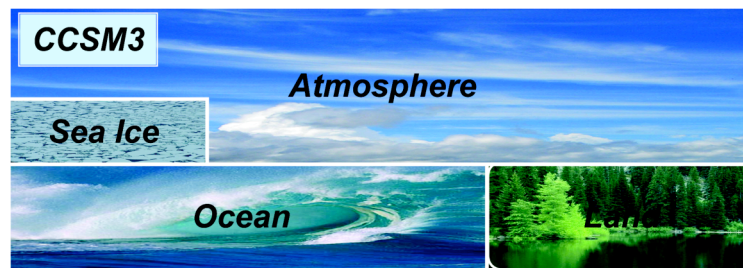
Figure 4.1: Components of the Community Climate System Model Version 3 (CCSM3), which include the atmosphere, ocean, land, and sea ice models. Adapted from Bette Otto-Bliesner.

The CCSM3 has three configurations, low (T31 X 3), intermediate (T42 X 1), and high (T85 X 1) resolutions. The model is run on an IBM SP4 system, which needs 62, 292, and 1146 CPU hours to simulate one year for the low, intermediate, and high-resolution configurations, respectively (Collins et al. 2006).

The Community Atmosphere Model (CAM3) is a three-dimensional primitive equation model of the atmosphere, with 26 levels in the vertical. The PMIP-2 paleoclimate simulations using CAM3 have an atmospheric resolution of T42, corresponding to a grid of 128 by 64 horizontal grid cells (approximately 2.8º resolution). The Community Land Model (CLM3) has the same resolution as the atmosphere grid spacing and includes land cover and plant functional types, prognostic soil and snow, and a river routing scheme. Grid boxes in CLM3 are divided into a hierarchy of land units, soil columns, and plant functional types. The land units have spatial patterns of heterogeneity and include glaciers, wetlands, urban areas, and vegetation.

NCAR's implementation of the Parallel Ocean Program (POP), developed at Los Alamos National Laboratory, is the ocean component of CCSM3 (Collins et al. 2006). The POP is a 3-D primitive equation model using the z-coordinate with 40 levels extending to a depth of 5.5 km. The PMIP-2 paleoclimate ocean simulations use a grid of 320 x 384 points; the poles of the "stretched" grid are located in Greenland and Antarctica. The horizontal resolution of POP is 1º by 1º latitude and longitude, with greater resolution in the Tropics and North Atlantic. The Community Sea Ice Model (CSIM5) is a dynamic-thermodynamic model that is equivalent to the POP in the horizontal. CSIM5 models sub grid scale ice thickness and elastic-viscous-plastic rheology. Elastic-viscous-plastic rheology describes the movement of the sea ice pack as

driven by ocean currents, winds, and the material strength of the sea ice pack (Hunke and Dukowicz 1997).

4.2   Experimental Design

Startup of the Pre-industrial simulation used initial conditions from year 300 of a Present Day control run (1990 control) of the CCSM3. Startup of the atmosphere and land models for the paleoclimate simulations used initial conditions from year 100 of the Pre-Industrial simulation (1750 control). The Pre-Industrial simulation was used for startup because the atmospheric trace gases are closer to, though still higher than, the concentrations estimated from ice cores for Last Glacial Maximum. Year 100 was chosen because the Pre-Industrial simulation was initialized from Present Day control and needed 100 years for variables to equilibrate. Initial conditions for the NCAR POP were taken from a previous CSM 1 LGM simulation. Anomalies of the ocean 3-D potential temperature and salinity fields were applied to initialize the ocean (Shin et al. 2003). This allows for a shorter spinup phase by starting with a previous LGM simulation that had reached quasi-equilibrium. This is good, because the ocean can take thousands of years to equilibrate. CSIM startup used Present Day initial conditions because of constraints on how the sea ice model can be started.

Two simulations were used in this study to analyze the climates of the Last Glacial Maximum and Pre-industrial. The Last Glacial Maximum and Pre-Industrial simulations both ran for 400 years. Output from the CCSM3 simulations were monthly means for 400 years. Mean climate results are for the last 100 years of each simulation.

Continental ice sheet extent and topography for the LGM CCSM3 simulation are from ICE-5G (VM2) ice sheet reconstruction (Peltier 2004). ICE-5G is a global ice sheet

reconstruction model that incorporates the global process of glacial isostatic adjustment (GIA). This process occurs when variations in the Earth's mantle and gravitational field are compensated by changes in external surface loads (i.e., continental ice sheets and glaciers), particularly during glaciation and deglaciation. Research has been extended to apply the mathematical models to resolve continental ice sheet thickness at Last Glacial Maximum through GIA theory, based on the history of relative sea level change. LGM occurred during the last glacial period and is within the time frame of radioactive carbon dating (^{14}C), so that geological history can be inferred. Through GIA and radioactive carbon dating, RSL history can provide important information of deglaciation history.

ICE-5G reconstructs land-based ice sheets and focuses on the ice sheet complexes of North America, Europe, Greenland, and Antarctica. Main features of each complex will be discussed briefly here; a more thorough description can be found in Peltier (2004). The Laurentide Ice sheet located over North America had a greater thickness over the James Bay, Keewatin, and Foxe Basin regions, with its central dome west of the Hudson Bay in the Keewatin region. The Laurentide Ice Sheet merges in western North America with the Cordilleran Ice Sheet, west of the Continental Divide, and extends into Alaska. These ice sheets cover present-day Canada and the northern United States.

The ice sheets of Europe were smaller than those of North America. The Fennoscandian ice sheet glaciated most of the Scandinavian region, with its central dome located over the northern end of the Gulf of Bothnia. The ice sheet of Antarctica is divided into the East and West Antarctic ice sheets separated by the Transantarctic Mountains. Greenland's ice sheet is thickest in central Greenland.

Figure 4.2 shows the topography difference in meters for LGM minus PI. The Laurentide ice sheet over North America has a maximum elevation of 3500 meters in the region of the Keewatin Dome. The Gulf of Bothnia between Finland and Sweden is region of maximum elevation for the Fennoscandian ice sheet approximately 1200 meters. The West Antarctic ice sheet had an elevation at LGM 1200 meters higher than its elevation at PI.
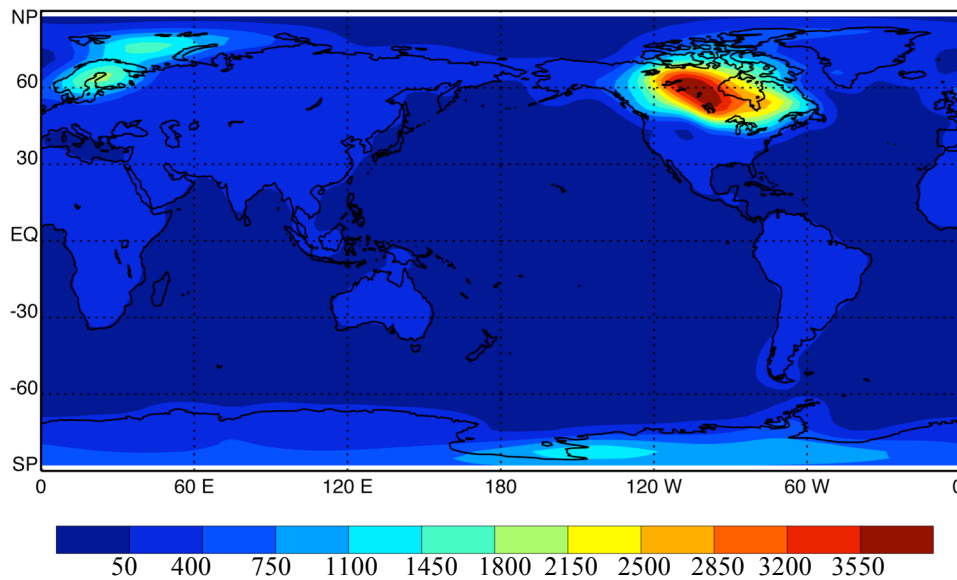
Figure 4.2: Simulated topography difference in meters for LGM minus PI.

There is a lowering of sea level by approximately 120 m, which was determined from ICE-5G reconstructions. Due to the lowering of sea level, land is exposed. The exposed lands include the land bridge between Asia and Alaska, through the Indonesian Archipelago, between Australia and New Guinea, and from France and the British Isles to Svalbard and the arctic coastline of Eurasia (Otto-Bliesner et al. 2006a). Present Day bathymetry is used in all LGM ocean regions, except for regions with relatively shallow sills like the Strait of Gibraltar and Denmark Strait, which are raised by approximately

29

120 m. These shallow sills are thought to be important in water mass formation. This was suggested during PMIP-2.

Forcings and boundary conditions in these simulations follow the protocols established by the second phase of the Paleoclimate Modeling Intercomparsion Project (PMIP-2 2008), as described below.

Forcings for Pre-industrial were set to appropriate conditions before industrialization, nominally at about 1800 A.D.. The solar constant for both LGM and Pre-industrial CCSM3 simulations was set to 1365 W m^{-2}. Atmospheric aerosols are set to Pre-industrial values in both simulations. The most important forcings for LGM are due to large changes in ice sheets, greenhouse gases, aerosols, sea level, and vegetation, and not the insolation changes (Otto-Bliesner et al. 2006a). Concentrations for atmospheric greenhouse gases (GHG) were based on ice core measurements and are significantly different between LGM and Pre-industrial (Table 4.2). The concentrations of atmospheric GHG are decreased relative to PI, resulting in a total decrease in radiative forcing of the troposphere 2.76 W m^{-2}. The majority of the change results from a decrease of CO_2 (Otto-Bliesner et al. 2006a). PMIP-2 simulations neglect changes in dust and vegetation, which could potentially have a large impact regionally in the LGM simulation. It is estimated that if dust were incorporated the resulting global forcing would be -1 W m^{-2} (Braconnot et al. 2007).

Table 4.2: Differences in ice sheets and atmospheric trace gases between the LGM and PI simulations. Adapted from Braconnot et al. 2007.

	Ice Sheets	Topography Coastlines	CO_2 (ppmv)	CH_4 (ppbv)	N_2O (ppbv)
0 ka	Present	Present	280	760	270
21 ka	ICE-5G	ICE-5G	185	350	200

CHAPTER 5

Simulated Mean Climate

In this chapter the mean climate global changes are presented followed by a discussion of the differences between the Last Glacial Maximum and Pre-Industrial Climates. The final section discusses the Pre-Industrial climate in relation to the Present Day climate.

5.1 Temperature
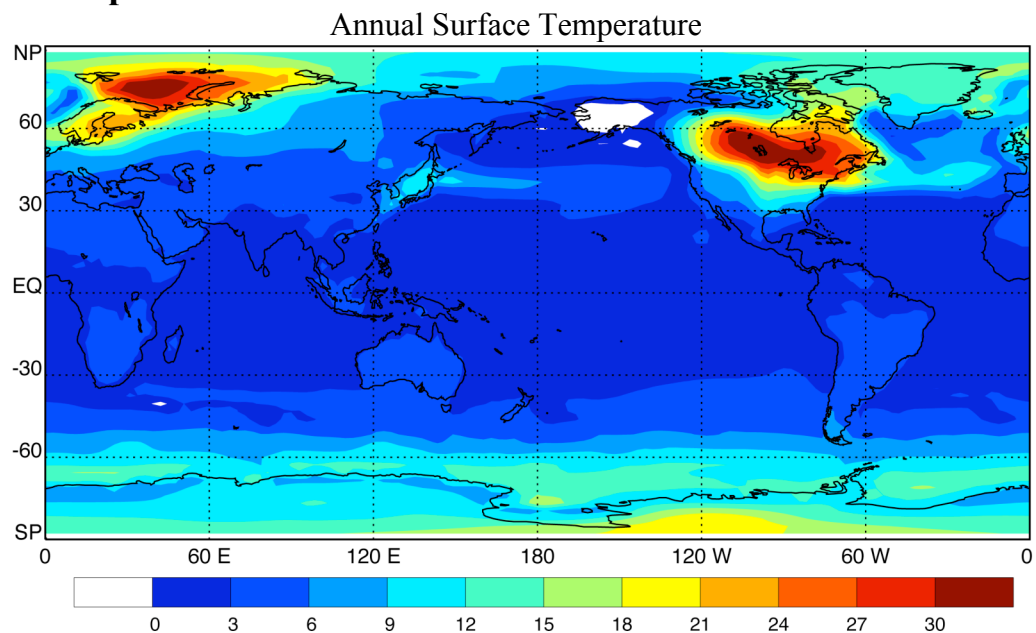
Figure 5.1: Annual surface temperature (K) difference for PI minus LGM.

The simulated annual surface temperature difference for PI minus LGM is shown in Figure 5.1. Greatest increases in temperature from LGM to PI are found in the high latitudes of both hemispheres. The greatest warming, of 30 K, is found in regions of the Laurentide and Fennoscandian ice sheets. In Alaska there is a decrease in temperature at PI, which occurs as a result of a deeper Aleutian Low at LGM. The surface winds associated with the deeper Aleutian low lead to enhanced advection of warmer air poleward into Alaska and the Gulf of Alaska. In the Southern Ocean, warming exists where sea ice has melted from LGM to PI. There is a much smaller change in surface temperatures in the tropics, and the tropical sea surface temperature change is on the order of 1.72 K warmer at PI. Globally averaged, the simulated annual surface temperature is 280.9 K at LGM and 285.8 K at Pre-Industrial, implying in a global warming of 4.9 K.
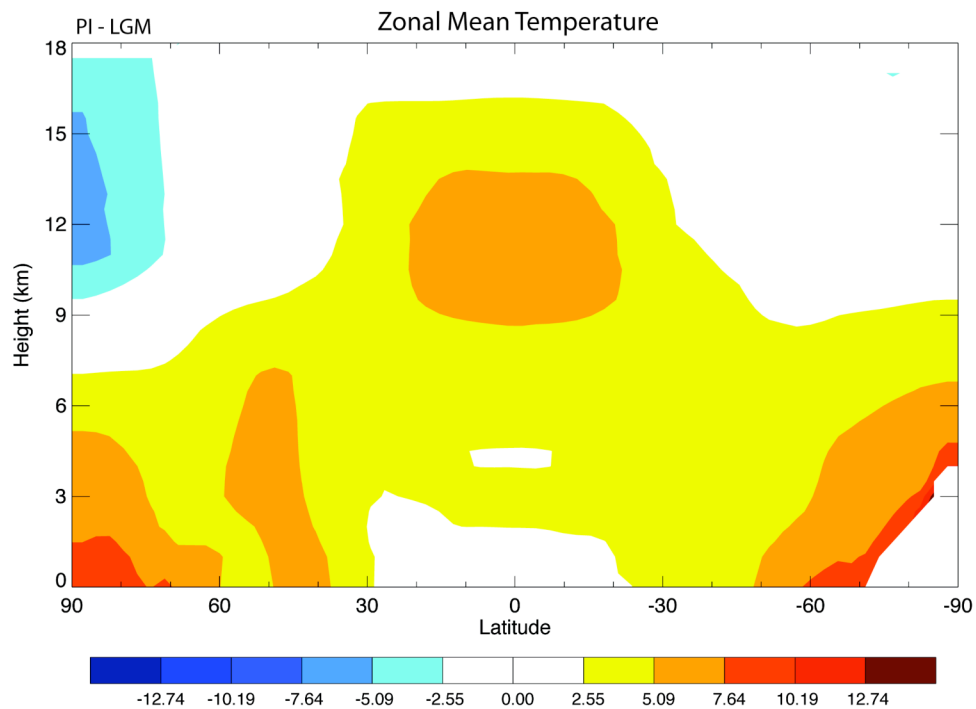
Figure 5.2: Annual zonal mean temperature in Kelvin for Pre-Industrial minus LGM.

The zonal mean temperature for Pre-Industrial minus LGM is illustrated in Figure 5.2. At the surface there is warming at both poles, which occurs due to changes in both continental ice and sea ice area and thickness. In the tropics at the surface there is a smaller change between the two climates. Greater warming occurs in the upper troposphere at PI, due to increased convection in the tropics and a smaller moist adiabatic lapse rate, leading to a decreased lapse rate. Increased surface temperature at both poles, along with increased poleward energy flow, contribute to polar amplification. A more thorough explanation of polar amplification is discussed in Chapter 6.

5.2   Sea Ice

There were significant changes in the amount of simulated sea ice in both hemispheres between the LGM and PI. Figures 5.3 and 5.4 show the sea ice area and thickness for the Northern and Southern Hemisphere maxima in March and August, respectively. The seasonal cycle of sea ice is driven by the annual cycle of solar radiation that reaches the Earth's surface and lags the annual cycle of the sun by a few months. From this, the sea ice maximum occurs at the end of the winter cold season, which is March for the Northern Hemisphere and August for the Southern Hemisphere.

There is a significant decrease in the amount of sea ice in the Southern Hemisphere, but paradoxically there is more sea ice in the Northern Hemisphere at PIdue to less land exposure in the Arctic Ocean at Pre-Industrial. Northern Hemisphere sea ice area increased from 11.16 to 13.00 (10^6 km^2) from LGM to PI. These results are those of Otto-Bliesner et al. (2006a). It should be noted that the annual sea ice area for both hemispheres was computed by averaging the amount of ice area annually in the extratropics (20º-90º N).

There are obvious differences in the amount of land exposed and the extent of sea ice in the Northern Hemisphere in Figure 5.3. In the Southern Hemisphere there are significant sea ice differences around Antarctica. The Arctic Ocean in both simulations is completely ice covered, with an expanded Arctic Ocean at Pre-Industrial. At LGM, sea ice extends eastward into the North Atlantic and North Pacific Oceans. Increased North Atlantic and equatorward extent of sea ice, down to 50ºN annually and 45ºN in winter, causes a southward shift of the Gulf Stream and storm tracks. Sea ice area in the Southern Hemisphere extends to the tip of South America (~ 45º S) and retreats dramatically at Pre-Industrial. In the North Atlantic, sea ice extends down to approximately 45º N. At Pre-industrial, there is significantly less sea ice and the ocean is ice-free below 55ºN in the North Atlantic.

In Figure 5.4, thickest sea ice at LGM of 6-7 meters is found over the Arctic Ocean and thinnest ice is collocated on the ice boundaries. PI sea ice thickness is largest over the Arctic, but is 1-2 meters less than at the LGM. Sea ice throughout the rest of the Northern Hemisphere is less than 2 meters thick.
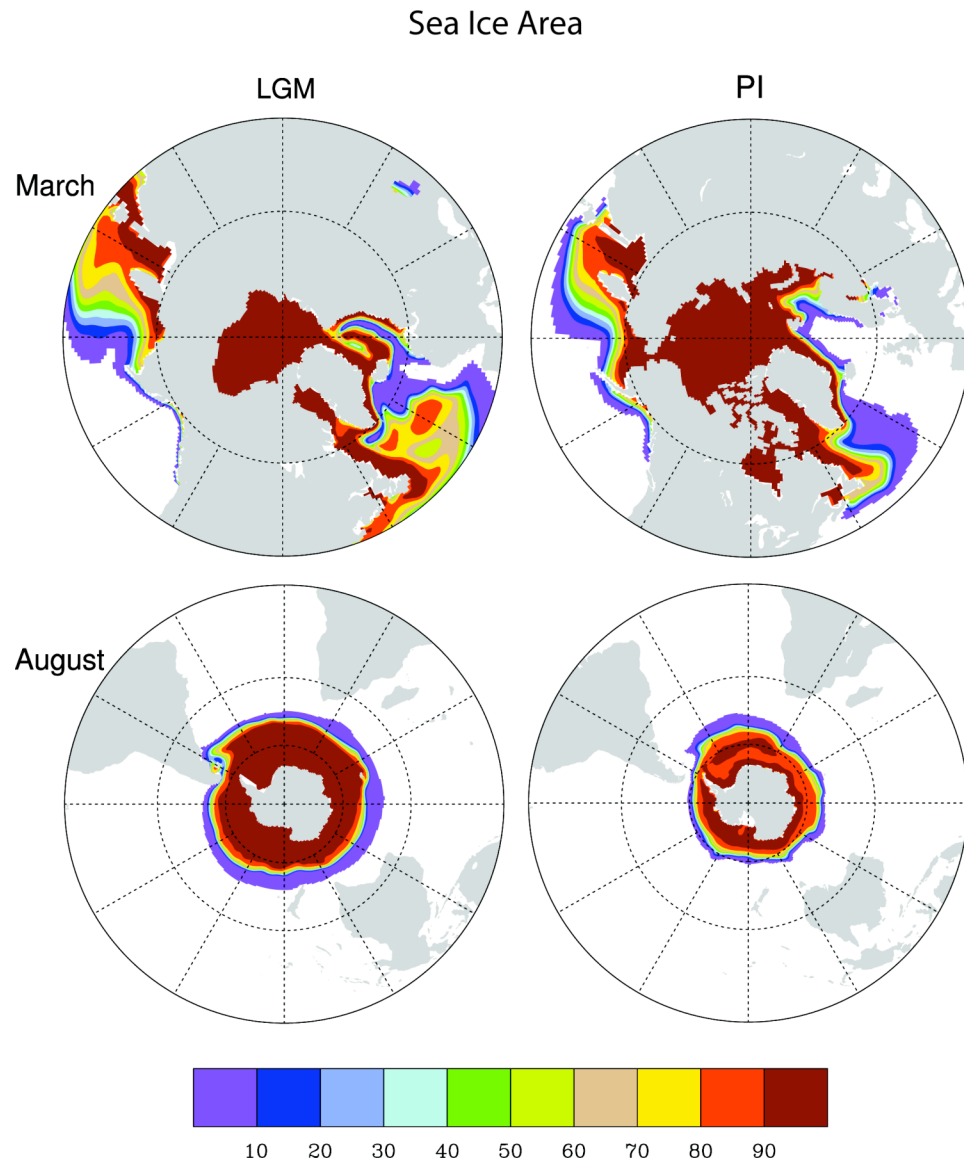
Sea Ice Area

Figure 5.3: Sea Ice Area (percent) simulated by the CCSM3 for the LGM (left) and PI (right). The months of March and August were selected because they are the months in which the maximum extent of sea ice in the Northern and Southern Hemispheres occurs, respectively.
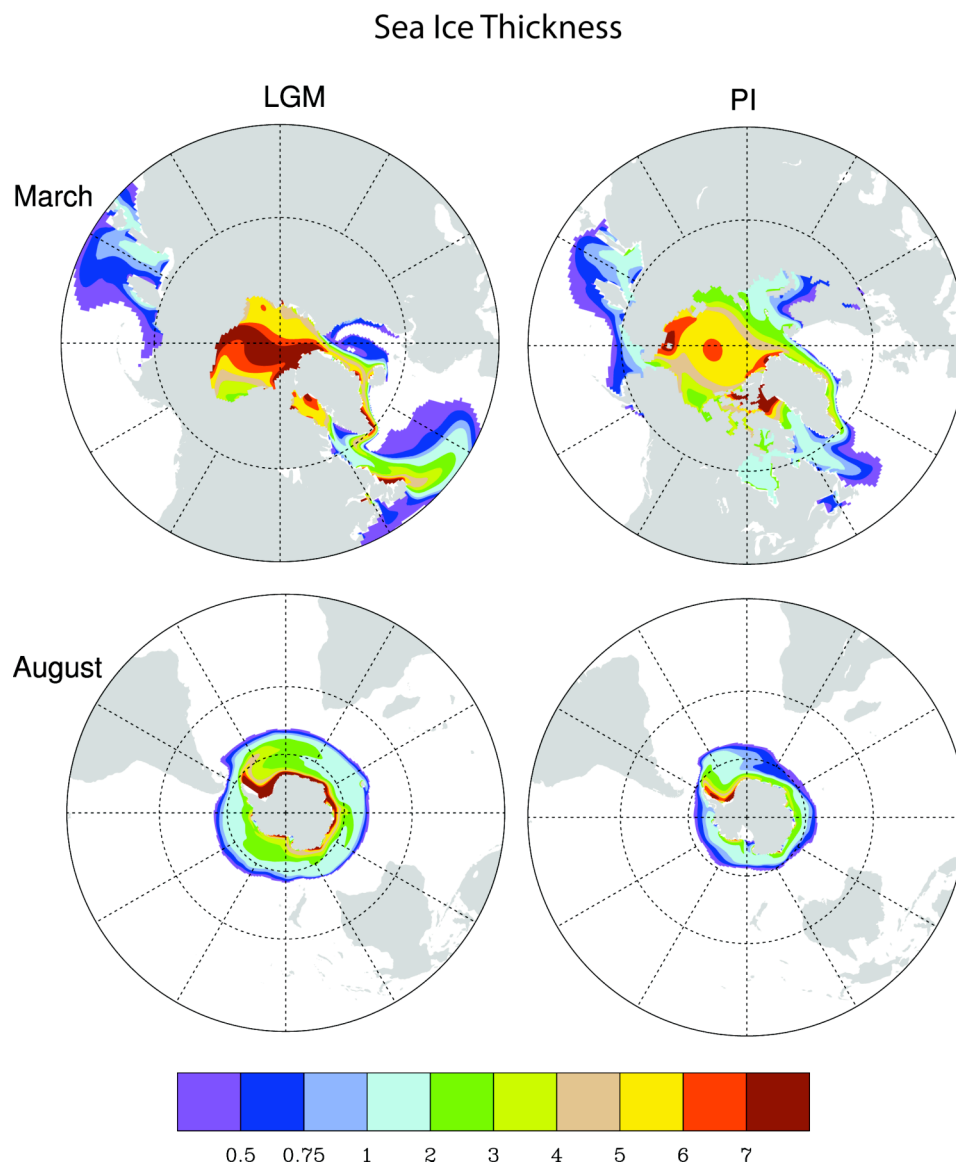
Sea Ice Thickness

Figure 5.4: Sea Ice Thickness (meters) simulated by the CCSM3 for the LGM (left) and PI (right The months of March and August were selected because they are the months in which the maximum extent of sea ice in the Northern and Southern Hemispheres occurs, respectively.

5.3   Hydrological Cycle

Annual precipitation for the two simulations is illustrated in Figure 5.5. At both LGM and PI there are maxima in precipitation off the coasts of Eastern Asia and the United States, with greater intensity at PI. In the tropics, a maximum occurs in the warm pool region of the Western Pacific Ocean, which extends into the Indian Ocean, as well as a maximum in the equatorial region of Western Africa. Increased precipitation also exists in the Amazonian basin. Along the Intertropical Convergence Zone (ITCZ) there is an increase in precipitation with a dry tongue directly over the Equator.

Figure 5.5: Annual precipitation in mm day^{-1} simulated for LGM (top left) and PI (top right) and PI minus LGM (bottom) by CCSM3.

38

A further look into precipitation changes over North America is given in Figure 5.6. There are precipitation increases of up to 2 mm day^{-1} where the Laurentide Ice Sheet was located and downwind at the ice sheet margin. A precipitation maximum also exists over Western Canada, with more precipitation at PI. Precipitation is usually greatest on the upwind side of a mountain because the air is forced upward there. On the downwind size there is a rain shadow effect. Once the large ice sheets have melted, more precipitation occurs in the region that had previously been downwind. Increased precipitation occurs at the ice sheet margin due to enhanced baroclinicity as a result of the temperature gradient that forms between the ice sheet and the surrounding land. This is comparable to the results of Manabe and Broccoli (1985).

A pronounced northward shift in the location of intense precipitation off the eastern U.S. coast at PI is associated with increased baroclinicity and a shift of the North Atlantic storm tracks. Decreased sea ice in this region also has an impact on the Gulf Stream in the North Atlantic. Increases in precipitation in the trade winds regions are found at PI due to increased winds near the surface.

Annual Precipitation
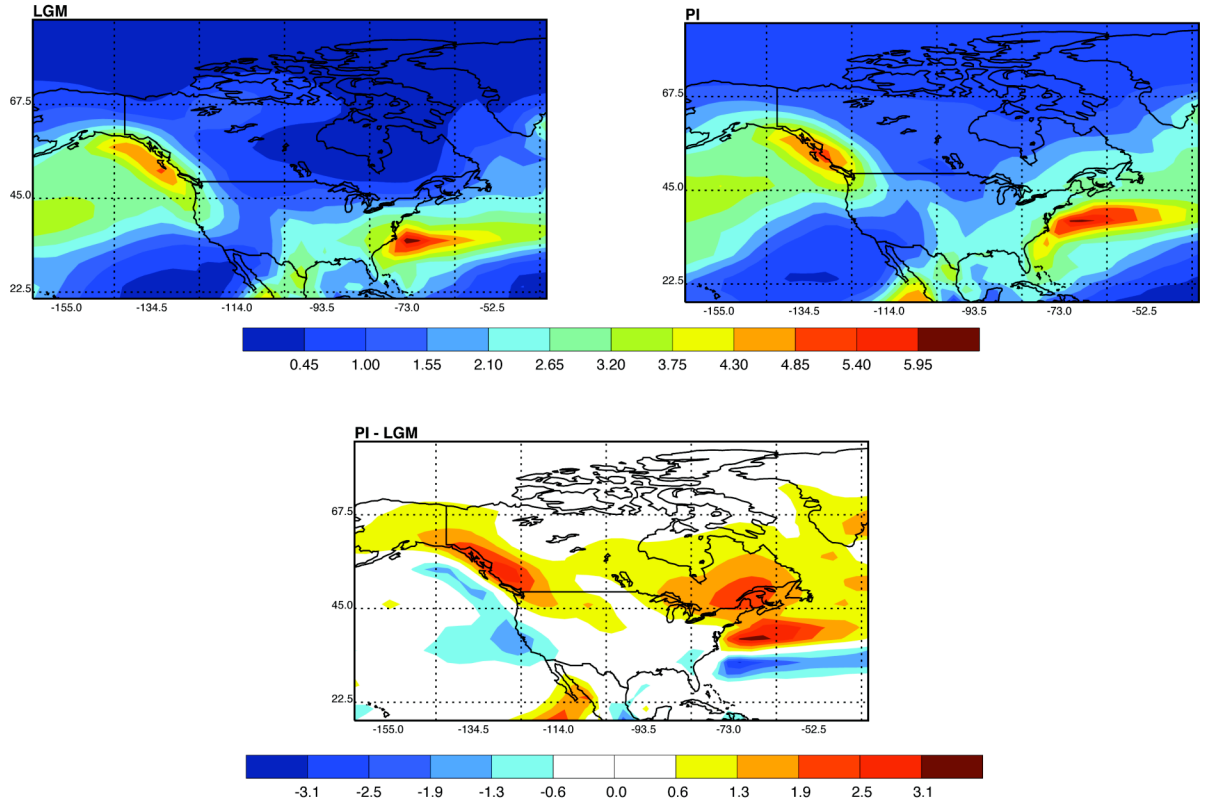
Figure 5.6: Annual precipitation for North America in mm day^{-1} simulated for LGM (top left) and PI (top right) and PI minus LGM (bottom) by CCSM3.

Evaporation changes illustrated in Figure 5.7 are very similar to the precipitation changes shown previously. At PI, there is increased evaporation of 2 mm day^{-1}, where the Laurentide Ice Sheet was located. There are also significant increases in evaporation below 40ºN where sea ice was located at LGM. Looking at the bottom panel of Figure 5.6, which have PI minus LGM, there is increased evaporation downwind of the Laurentide Ice Sheet. Off the eastern United States, there are large increases of evaporation where sea ice was located at LGM and decreases just south of that region due to a northward shift of the storm tracks at PI.

Annual Evaporation

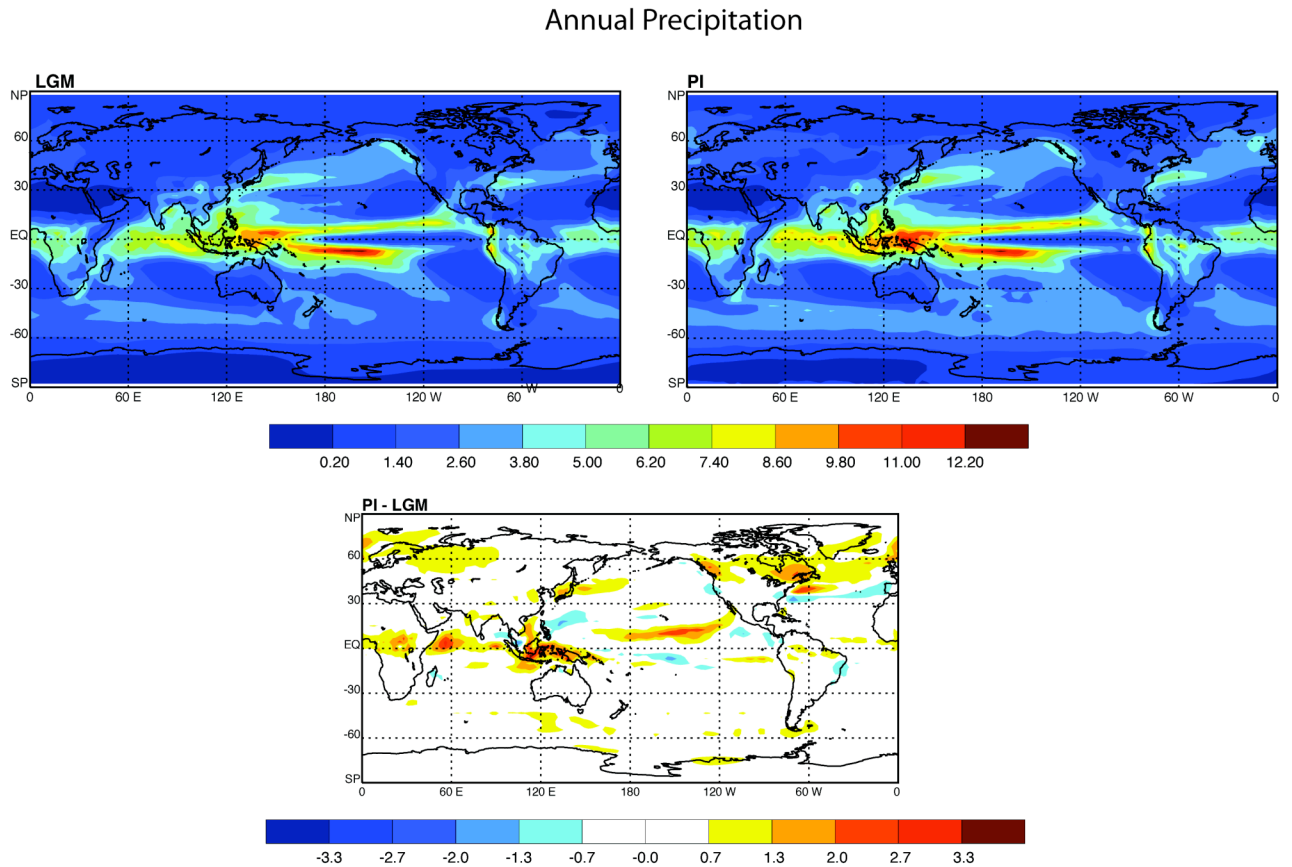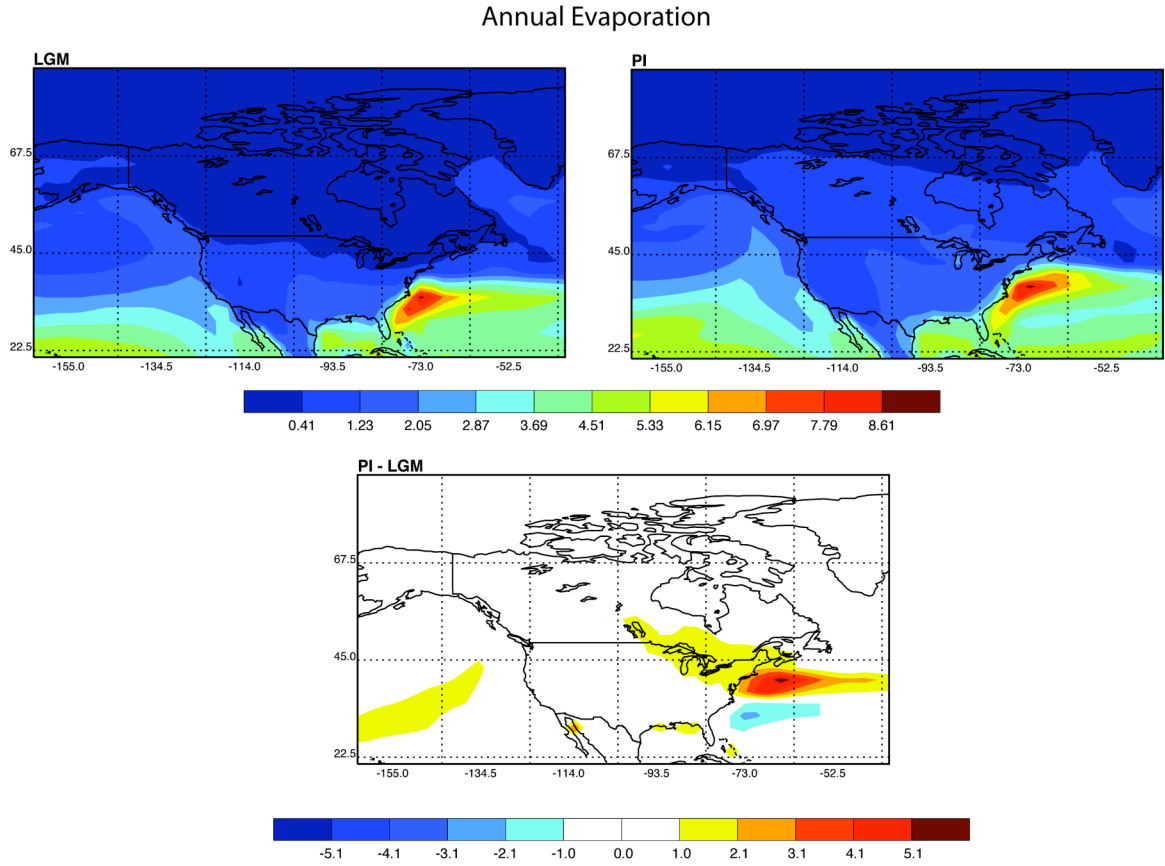
Figure 5.7: Annual evaporation in mm day^{-1} simulated for LGM (top left) and PI (top right) and PI minus LGM (bottom) by CCSM3.

The globally averaged precipitable water is shown in Figure 5.8. There is a large decrease in the amount of precipitable water at LGM compared to PI. Precipitable water is 17.6 kg m^{-2} at LGM and 21.9 kg m^{-2} at PI, yielding a 20% increase. The greatest increases are in the tropics, as expected from the Clausius Clapeyron relation, and also where the ice sheets melted. Increased precipitable water where the ice sheets melted occurs due to both more free air (approximately 3500 meters worth) and warmer temperatures.

Annual Precipitable Water
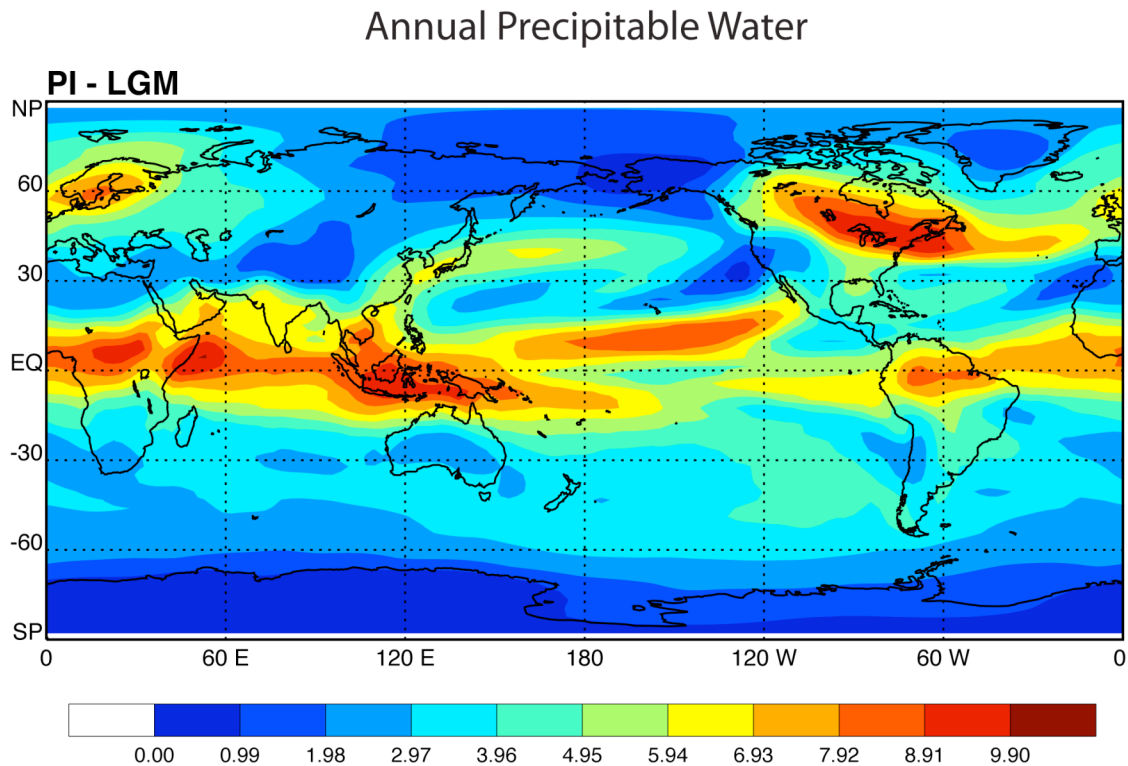
Figure 5.8: Annual precipitable water in kg m^{-2} simulated for PI minus LGM.

5.4   How is the Pre-Industrial climate different from Present Day?

Anthropogenic changes within the climate system have occurred since the Industrial Revolution; therefore, the Present Day climate is becoming increasingly different from the Pre-Industrial climate. This section emphasizes the significant changes since Pre-Industrial.

There has been a dramatic increase since 1750 A.D. of atmospheric trace gases, as seen in Table 5.1, which results in a net radiative forcing of 1.5 W m^{-2} (Ramasawamy et al. 2001). That is nearly half of the radiative forcing from Last Glacial Maximum to Pre-Industrial, discussed previously in Chapter 4.

Table 5.1: Forcings for Pre-Industrial and Present Day climates.

	Pre-Industrial	Present Day
CO_2	280 ppm	355ppm
CH_4	760 ppb	1714 ppb
N_2O	270 ppb	311 ppb
CFC_{11}	0	283 ppt
CFC_{12}	0	503 ppt
Solar constant	1365 W m^{-2}	1367 W m^{-2}

Carbon dioxide has increased by 30%, nitrous oxides have increased by 15%, and methane has more than doubled in concentration. As expected, increases in these atmospheric trace gases result in tropospheric warming. Table 5.2, adapted from Otto-Bliesner et al. (2006b), presents annual means for CCSM3 simulations of Pre-Industrial and Present Day. From Table 5.2, it is evident that the Present Day climate conditions are wetter and warmer than the Pre-Industrial climate. Reductions in sea ice area have occurred in both hemispheres, resulting in more evaporation. These changes, along with increases in temperature and precipitation, result from the impact of humans within the 20th century. Future changes will be on the order of this change if not greater.

Table 5.2: Annual means simulated for the climates of Pre-Industrial and Present Day (Adapted from Otto-Bliesner et al. 2006b).

	Pre-Industrial	Present Day
Global		
Precipitation (mm day^{-1})	2.74	2.79
Surface Latent Heat (W m^{-2})	79.99	81.48
Precipitable water (mm)	22.19	24.13
Surface Temperature (^{o}C)	13.52	14.80
Extratropics (20 - 90°)		
NH sea ice area (10^6 km^2)	13.35	11.07
SH sea ice area (10^6 km^2)	16.01	13.94

5.5   Summary

Results shown in this section indicate that the Pre-Industrial climate was warmer and wetter than the climate of the Last Glacial Maximum. Table 5.3 summarizes some annual mean variables discussed in this chapter.

Table 5.3: Global annual means simulated for Last Glacial Maximum and Pre-Industrial in CCSM3.

	LGM	PI
Annual		
Surface Temperature (K)	280.90	285.80
Precipitation (mm day^{-1})	2.44	2.73
Precipitable water (kg m^{-2})	17.60	21.90
NH sea ice area (10^6 km^2)	11.61	13.34
SH sea ice area (10^6 km^2)	34.37	16.58

Surface temperatures are 5 K greater at PI than at the LGM. Annual mean precipitation and evaporation are 0.33 mm day^{-1} more at PI than the simulated average of 2.44 mm day^{-1} at LGM. There is increased precipitable water globally by 4.35 kg m^{-2} at Pre-Industrial compared to the Last Glacial Maximum. A significant decrease in the

amount of sea ice occurs in the Southern Hemisphere, but more sea ice is present in the

Northern Hemisphere due to more land exposed in the Arctic Ocean. A northward shift

in the Gulf Stream of the North Atlantic at PI due to decreased sea ice and a shift in

baroclinic eddy activity. The upper troposphere is dramatically warmer at PI than the

LGM, leading to a decreased lapse rate.

A few questions that arise from results shown in this section are as follows. How

do the mean climate results affect climate feedbacks associated with the hydrological and

energy cycles? How do the feedbacks of the hydrological and energy cycles interact with

each other? Do these feedbacks act to amplify climate change? These questions will be

answered in Chapter 6.

CHAPTER 6

Analysis of Climate Feedbacks

This section focuses on how the hydrological and energy cycles change as a result of feedbacks within the climate system. Feedbacks are discussed as they relate to the simulated mean climate, discussed in Chapter 5. Other items addressed later in this section are how the energy and water cycle feedbacks interact with each other and whether the feedbacks amplify the climate change from Last Glacial Maximum to Pre-Industrial. The biogeochemical feedback will not be discussed here because it is not incorporated in the CCSM3 simulations.

6.1   Climate Feedbacks

Water vapor feedback:

Water vapor, discussed in Chapter 3, is the principal absorber of longwave radiation and is associated with the strongest feedback in the climate system. The Clausius Clapeyron equation

$$\frac{de_s}{dT} = \frac{L}{T(\alpha_2 - \alpha_1)} \tag{6.1}$$

predicts an exponential increase of saturation vapor pressure with temperature. In Eq. 6.1, where e_s is the saturation vapor pressure, T is temperature, L is the latent heat of the phase transition and α_1 and α_2 are the specific volumes of the two phases (Wallace and Hobbs 1977). This can be seen in the schematic in Figure 6.1.
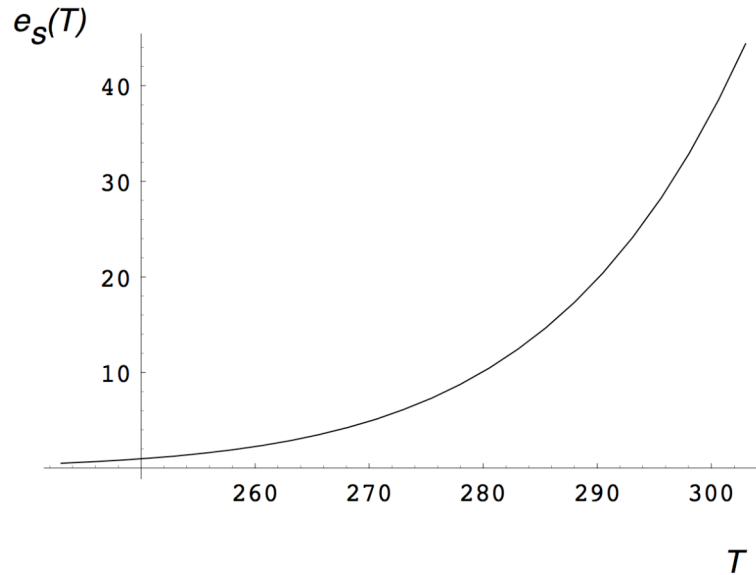
Figure 6.1: Schematic of the Clausius Clapeyron relation. This indicates the exponential increase of saturation vapor pressure as temperature increases.

Saturation vapor pressure is the vapor pressure that an air parcel has at saturation. It is solely a function of temperature. The higher the saturation vapor pressure, the more water vapor the atmosphere can hold. As temperature and the amount of water vapor in the atmosphere increase, more precipitation occurs. In the transition from the Last Glacial Maximum to Pre-Industrial, an increase in temperature led to a higher saturation vapor pressure, allowing more precipitable water and more precipitation. The increases in temperature, precipitation, and precipitable water are shown in Figures 5.1, 5.6, and 5.8, respectively. The increase in water vapor leads to a positive water vapor feedback and amplifies tropospheric warming.

Ice-albedo feedback:

Bony et al. (2006) discussed the feedbacks associated with the sea ice influence on climate and the net effect of sea ice changes that contribute to the amplification of polar warming. The most important sea ice feedback is the influence of the ice area and the surface albedo. From Chapter 3, we know that, as there is a reduction in sea ice due to melting, the surface becomes less reflective, and therefore the amount of solar radiation absorbed at the surface increases. This enhances the initial warming and is a positive feedback. Figure 5.3 displays the sea ice area for both the Northern and Southern Hemispheres at the LGM and PI. There is a significant decrease in the amount of sea ice area in the Southern Hemisphere from LGM to PI. In the Northern Hemisphere there is a reduction in sea ice area in the North Atlantic and Pacific at PI. Changes in sea ice extent and thickness affect the surface energy budget (e.g., sensible and latent heat fluxes) and result in a redistribution of heat in the system. Hall (2004) indicates that extent and thickness changes are responsible for the seasonal distribution of polar warming. Reductions in sea ice area and thickness in both hemispheres indicate that a positive ice albedo feedback occurs and from surface temperature (Figure 5.1) it is clear that there is stronger warming in the polar regions.

Lapse rate feedback:

The lapse rate feedback is the rate of decrease of temperature with altitude. Referring back to Figure 5.2, which shows the zonal mean temperature, there is a warming of 5 K in the upper troposphere at PI, compared to LGM. Upper tropospheric warming corresponds to a smaller moist adiabatic lapse rate. As mentioned in Chapter 3, the moist adiabatic lapse rate is the rate at which saturated air parcels cool as they rise. If

there is a smaller moist adiabatic lapse rate, parcels are not cooling as much and the lapse

rate is reduced. The reduced lapse rate allows the air at higher altitudes to warm more

than at the surface, as seen in Figure 5.2. A decreased lapse rate makes it easier for

warmer air aloft to radiate heat away to space, yielding a negative lapse rate feedback.

Cloud feedback:

Stephens (2005) states that atmospheric processes govern the cloud feedbacks.

This occurs via atmospheric circulations, cloudiness, and radiative and latent heating of

the atmosphere. As mentioned in Chapter 3, the cloud feedbacks are dependent on cloud

amount, cloud optical properties, and cloud top height. Because the large-scale

atmospheric circulation controls the occurrence of clouds, there is a large variety of cloud

systems that can occur from the tropics to the poles.

In the polar regions, clouds have a dramatic influence on the surface radiation

budget (Bony et al. 2006). Holland and Bitz (2003) found that there is a positive

correlation between an increase in polar cloud cover and polar amplification, which

suggests a positive polar cloud feedback. This is due to the local effect of clouds on the

downward longwave radiation at the Earth's surface.

In the low latitudes, boundary layer clouds cover a large fraction of the area. The

amount of low clouds in this region depends on synoptic and planetary scale factors (i.e.,

precipitation processes and changes in cloud thickness). Increases in low clouds in

warmer climates like Pre-Industrial are driven by stronger stratification due to increased

moist adiabats across the Tropics (Bony et al. 2006). This produces a strong negative

low cloud feedback.

The simulated vertically integrated high and low clouds are shown in Figures 6.2 and 6.3 for LGM, PI, and PI minus LGM. Cold, high clouds radiate less infrared radiation to space, therefore trapping more infrared (i.e., longwave radiation) in the atmosphere. In Figure 6.2, more high clouds are found at Pre-Industrial in regions where the ice sheets have melted or where there has been a decrease in the size of the ice sheet, in particular over central Greenland and the West Antarctic ice sheet. There are small increases of high clouds in the polar regions of the Northern Hemisphere. More high clouds also exist at PI in the tradewind zones, where precipitation has increased (refer back to Figure 5.6). Globally averaged, the vertically integrated high cloud fraction at PI has increased by 0.01.

Figure 6.2: Annual mean vertically integrated high cloud fraction simulated for Last Glacial Maximum (top left), Pre-Industrial (top right) and PI minus LGM (bottom).

The vertically integrated low cloud fraction has increased in the high latitudes of both hemispheres. The greatest increase of low clouds is found where the Laurentide ice sheet's central dome was located (i.e. west of the Hudson Bay). Increased low clouds are found in the stratocumulus regions off the western coasts of the United States and South America. This is comparable to what Kiehl et al. (2006) found in their global warming scenarios. Their study suggests that in global warming scenarios, more low clouds exist over the subtropical oceans, resulting in less warming (or a cooling). This is expected since low clouds have a cooling effect. Globally averaged, there is a slight increase in the vertically integrated low cloud fraction at PI.
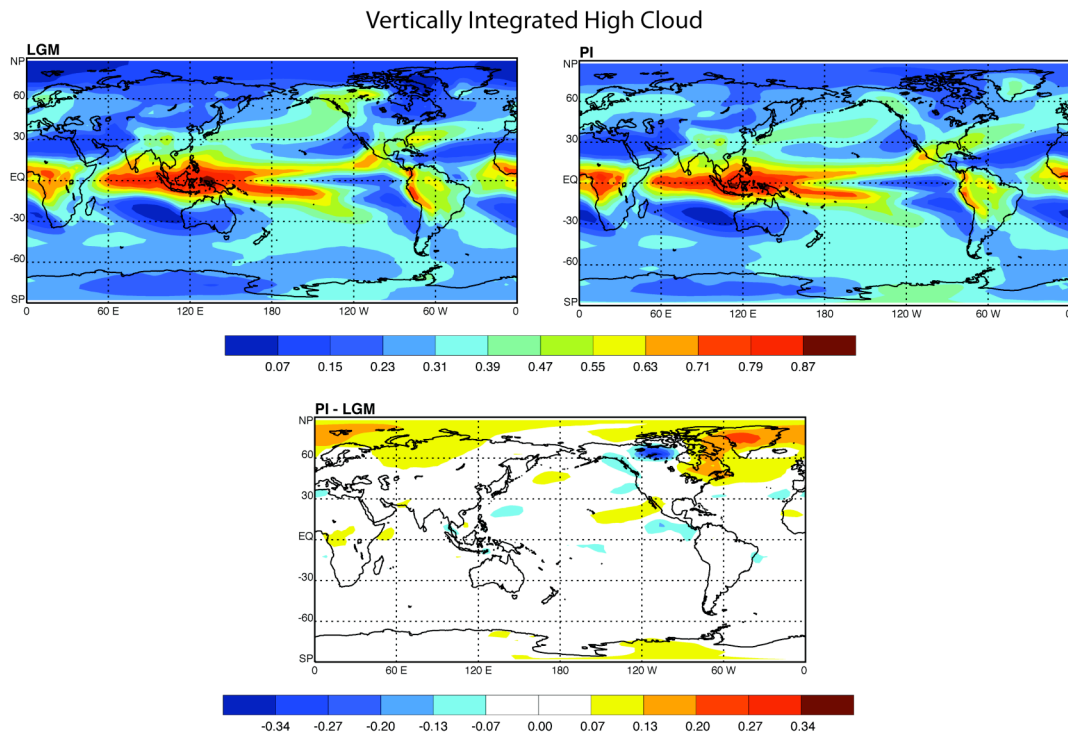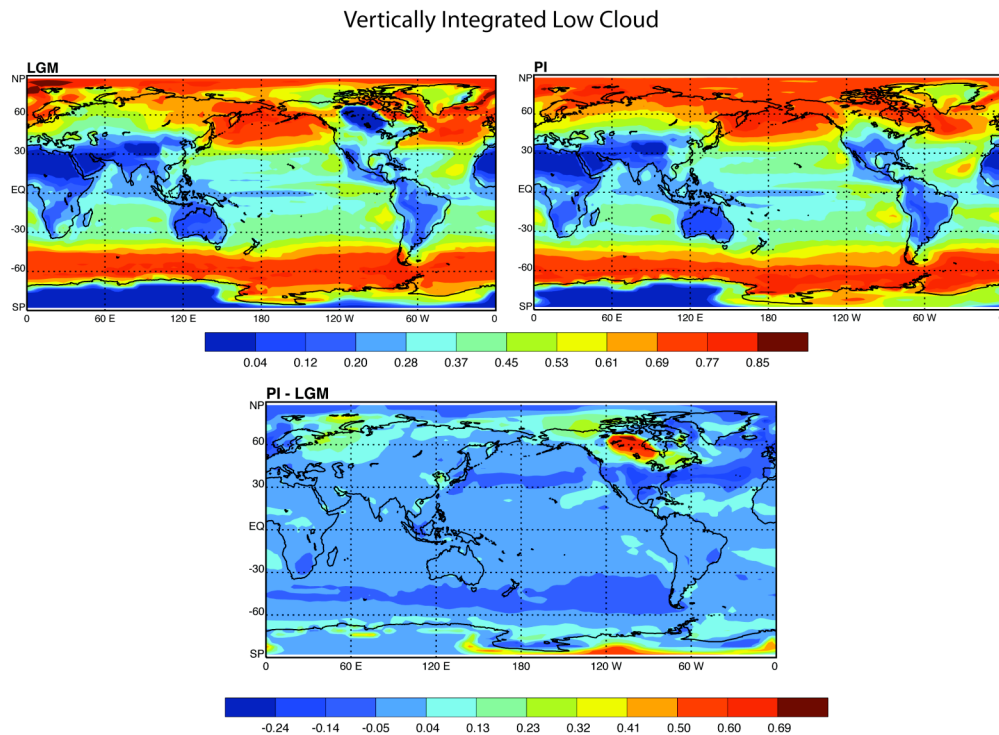

Figure 6.3: Annual mean vertically integrated low cloud fraction simulated for Last Glacial Maximum (top left), Pre-Industrial (top right) and PI minus LGM (bottom).

6.1.1   Cloud Forcing

Cloud forcing in the difference between the all-sky and clear-sky radiative fluxes and can be divinded into shortwave, longwave, and net. Shortwave cloud forcing (SWCF) is defined as the all-sky minus clear-sky shortwave radiation. In the shortwave, clouds tend to reduce the absorbed solar radiation due to a higher albedo than the underlying surface. This results in a cooling effect. The longwave cloud forcing (LWCF) is defined as the clear-sky minus all-sky longwave radiation. Clouds radiate the infrared radiation downward and act to warm the surface, resulting in a positive longwave cloud forcing. The net cloud forcing is the SWCF plus the LWCF. It is negative.

Figures 6.4 and 6.5 show the SWCF and LWCF for the Last Glacial Maximum, Pre-Industrial, and PI minus LGM. The locations of the ice sheets can be seen through the effects of the shortwave, because during the Last Glacial Maximum the clouds are over a lighter, brighter, highly reflective surface (i.e., the ice sheet) and therefore have a weaker effect. A weaker effect exists because if the clouds were not there, the ice-covered surface would still reflect the shortwave radiation. At LGM, there is weaker SWCF over the polar regions and greater SWCF in the storm tracks of the North Pacific and Atlantic. In the PI climate, there is stronger SWCF in the polar regions and slightly weaker SWCF in the storm tracks compared to the LGM. Globally averaged, shortwave cloud forcing is -49.77 W m^{-2} at LGM and -54.55 W m^{-2} at PI. Greater SWCF is expected at PI due to less reflective ice at PI.

The longwave cloud forcing for both LGM and PI is greatest in the equatorial Pacific, where the most high clouds and precipitation occur. This is expected because in the longwave clouds tend to reduce the emission to space, trapping heat in the

atmosphere, resulting in a warming due to clouds. Globally averaged, the LWCF is 28.46 and 29.42 W m^{-2} at LGM and PI, respectively.

The SWCF and LWCF balance each other in the winter hemisphere, but in the summer the negative shortwave cloud forcing dominates over the longwave cloud forcing and results in a cooling due to clouds. The change in net cloud radiative forcing associated with a change in climate is what governs the cloud feedback (Wielicki et al. 1995).

Shortwave Cloud Forcing
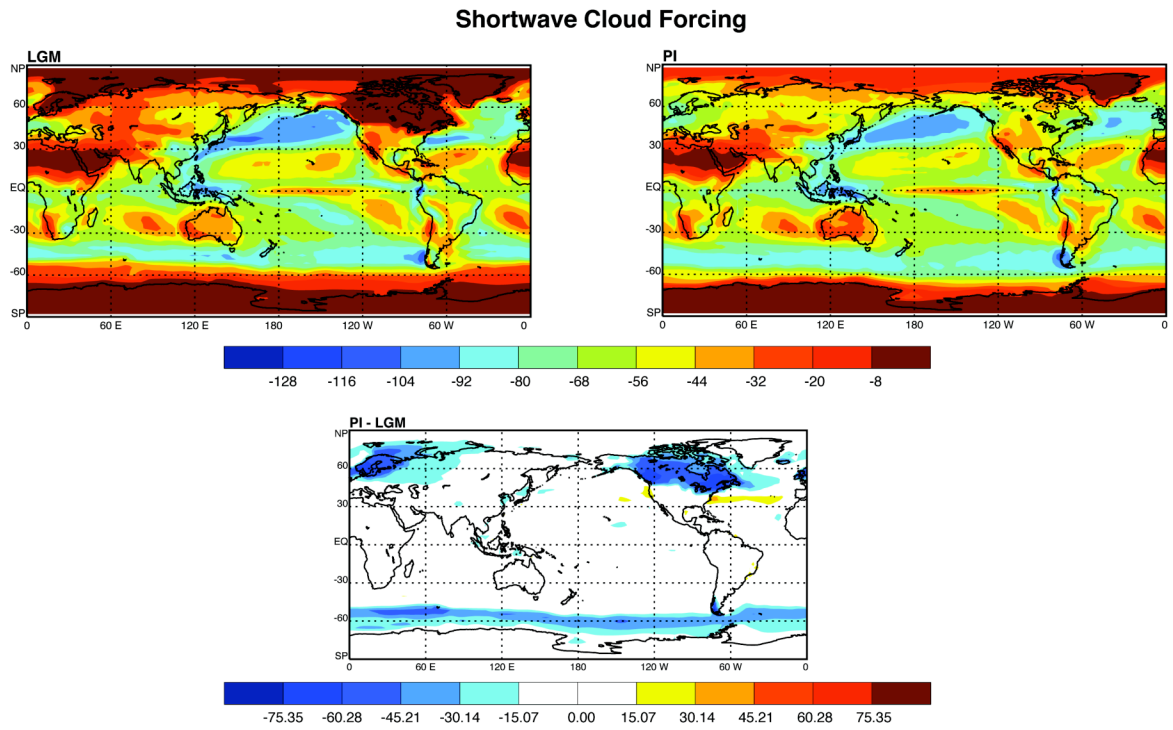
Figure 6.4: Shortwave cloud forcing in W m^{-2} at the top of model (TOM) simulated for Last Glacial Maximum (top left), Pre-Industrial (top right), and PI minus LGM (bottom).

Longwave Cloud Forcing

Figure 6.5: Longwave cloud forcing in W m^{-2} at TOM simulated for Last Glacial Maximum (top left), Pre-Industrial (top right), and PI minus LGM (bottom).

Net Cloud Forcing
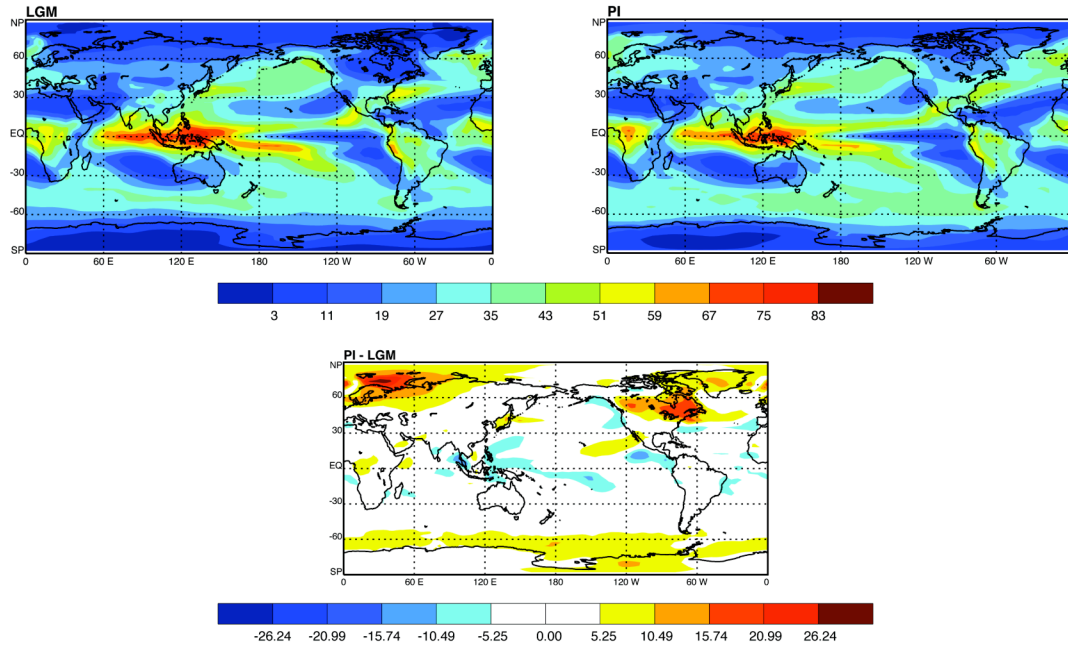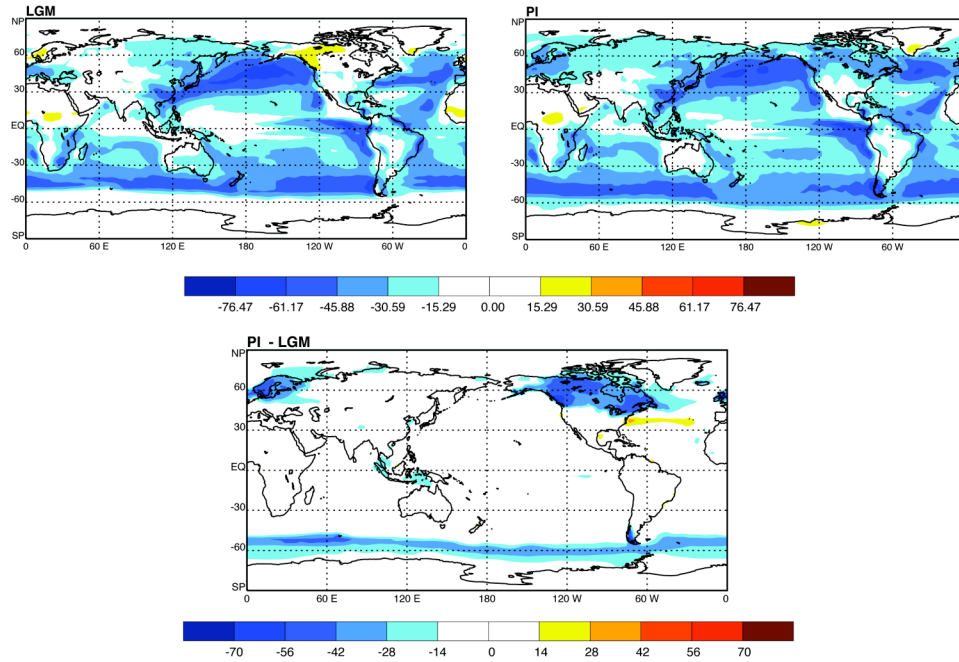

Figure 6.6: Net cloud forcing in W m^{-2} simulated for Last Glacial Maximum (left), Pre-Industrial (right), and PI minus LGM (bottom). The net cloud forcing at the top of model was computed by subtracting the clear-sky minus all-sky LW at the TOM from the all-sky minus clear-sky SW at the TOM.

54

Again, the location of the ice sheets can be seen through the effects of the shortwave radiation in net cloud radiative forcing (Figure 6.6). Less cooling occurs when the ice sheets are present, and more cooling when the ice sheets have melted. Off the west coast of continents, there is stronger cooling due to the low, thick clouds that reflect shortwave and cool the surface of the earth. At Pre-industrial, there is a stronger cloud effect in the Arctic and Antarctic regions due to decreased sea and land ice. For PI minus LGM, there is warming due to clouds in the storm tracks off the coasts of eastern Asia and the United States, which is due to regions of high thin cirrus that trap the outgoing longwave radiation and radiate it downward, warming the surface of the Earth.

Clouds have an influence on both the water balance of the atmosphere and Earth's radiation budget, and small variations can alter climate. Perturbations to the atmospheric radiation budget that occur via cloud changes in response to a climate forcing dictate the response of the global hydrological cycle and also suggest that cloud feedbacks are likely to control the precipitation efficiency associated with the response of the hydrological cycle (Stephens 2005). This interaction will be addressed later in this chapter.

6.2   What mechanisms contribute to polar amplification?

In most global warming simulations, polar amplification occurs mainly in the Northern Hemisphere. From the zonal mean temperature, Figure 5.2, it is evident that polar amplification from LGM to PI, i.e., from a colder to warmer climate occurs in both the Northern and Southern Hemispheres. Changes in snow and ice cover and their associated feedbacks are likely to be amplifiers of climate change (Masson-Delmotte et al. 2006). Holland and Bitz (2003) found that in future climate simulations, the Arctic amplification is 1.5-4.5 times the global warming. The level of polar amplification is

dependent on sea ice thickness and snow cover. This section will concentrate on the mechanisms behind polar amplification in the Southern Hemisphere.

Cai (2005) discussed the dynamical amplification of polar warming using a 4-box coupled atmospheric-surface moist radiative-transportive climate model. Local thermodynamic feedbacks contribute to a relatively large surface warming at high latitudes through the ice-albedo feedback, which amplifies this warming at high latitudes. In the low latitudes, the evaporation feedback, where convective activity enhances evaporation and decreases solar radiation, acts to strongly damp surface warming. With the ice albedo and water vapor feedbacks, Cai (2005) suggests that poleward heat transport can lead to an amplification of polar temperatures. Polar amplification due to increased poleward heat transport occurs due to a redistribution of surplus energy (e.g., an increase in net radiation) from the low to high latitudes and by an enhanced water vapor feedback in the high latitudes. The dynamical amplifier of polar amplification requires the net increase of poleward heat transport in response to an anthropogenic radiative forcing. In a global coupled climate model, the net radiation surplus and deficit would occur at the top of the model. Since PI is a warmer climate than LGM, there is a surplus of energy in the tropics due to increased precipitable water, which therefore must be distributed to the poles of both hemispheres.

6.2.1 How can the ocean contribute to polar amplification?

The oceanic thermohaline circulation, sometimes referred to as the meridional overturning circulation, has an important role in global climate. Paleoclimate records suggest that at Present Day the thermohaline circulation has a strong North Atlantic Deep Water (NADW) and a moderate Antarctic Bottom Water (AABW), whereas at LGM the

56

NADW is shallower and weaker (Shin et al. 2003). Figure 6.7 shows the Atlantic Ocean

Meridional Overturning Circulation. At LGM the meridional overturning circulation is

shallower and weaker than at PI. This is in agreement with Shin et al. (2003) and Otto-

Bliesner et al. (2006a). Sea ice changes in the Southern Ocean have a significant role in

modulating the overturning circulation. The Southern Ocean control of the NADW

circulation is caused by greater sea ice sensitivity to the LGM conditions in the Southern

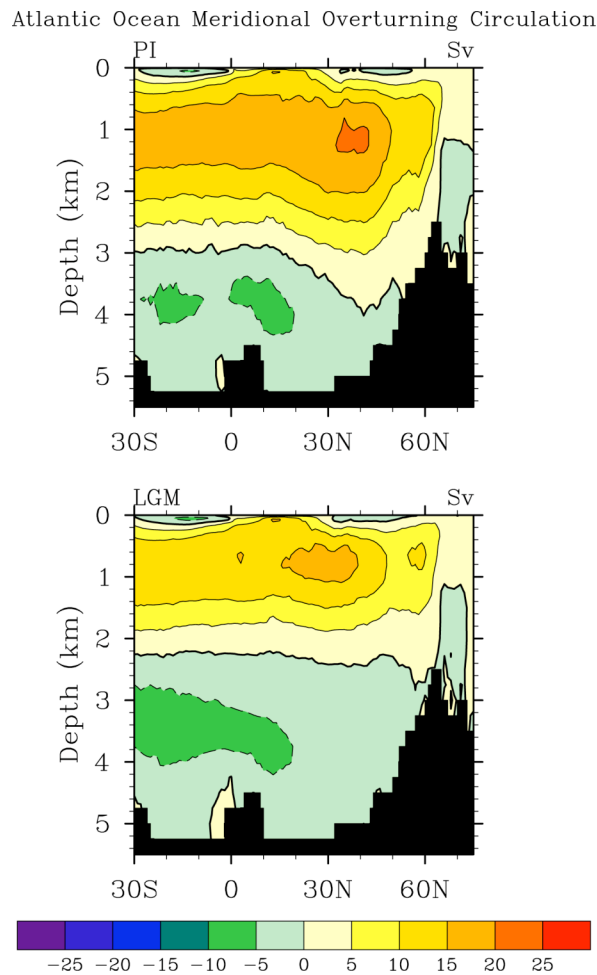Ocean than in the North Atlantic (Shin et al. 2003).

Figure 6.7: Atlantic Ocean Meridional Overturning Circulation for Pre-Industrial (top) and Last Glacial Max (bottom) simulated by CCSM3.

From Figures 5.3 and 5.4, there is a decrease in sea ice area and thickness in the Southern

Ocean from LGM to PI. Shin et al. (2003) determined that the sea ice in the Southern

Ocean is significantly thinner than ice in the North Atlantic as a result of deep convective mixing, which prevents the thickening of sea ice. Due to deep convective mixing and thinner sea ice, this allows for ice to melt easier, leading to a reduced surface albedo and more warming. Open ocean on the equatorward side further favors wind-driven spread of sea ice due to increased westerlies in the Southern Ocean (Shin et al. 2003). As a result, sea ice covered area is almost doubled at LGM (see Figure 5.3).

From the mechanisms mentioned in this section, poleward heat transport and ocean thermohaline circulation changes, it is evident that polar amplification can occur in both the Northern and Southern Hemispheres.

6.3 How do the energy and water feedbacks interact with each other?

Atmospheric radiative cooling is the combined net radiative energy flux at the top of the atmosphere with the net radiative flux at the Earth's surface. There is a well-known relationship between the globally averaged rate of atmospheric radiative cooling and the global-mean precipitation rate (e.g., Stephens et al. 1994; Sugi et al. 2002). Two feedbacks that link the hydrologic cycle and the atmospheric radiative cooling are the radiative dynamical convective feedback (RDC) and the global radiative convective feedback (GRC). The RDC feedback is a positive feedback between the radiative warming and cooling gradients associated with high clouds produced by deep convection and large scale rising motions (e.g., Slingo and Slingo 1988, Randall et al. 1989). The GRC feedback is a negative feedback where stronger convection leads to more high clouds, which tend to reduce the atmospheric radiative cooling and further reduce the precipitation rate (Fowler and Randall 1994).

Figure 6.8 shows that there is stronger atmospheric radiative cooling at Pre-industrial than at Last Glacial Maximum. This is expected in part because in a warmer climate there is more water vapor in the air. The increased global-mean radiative cooling results in an increase of global-mean precipitation, which can be seen in Figure 6.9, which shows the globally averaged atmospheric radiative heating versus the globally averaged latent heating.

To get an idea of the cloud radiative effects, the all-sky and clear-sky effects on radiative cooling of the atmosphere are shown. There is a greater difference between all-sky and clear-sky for PI, indicating that the clouds are having a greater effect. The change in cloud radiative forcing tends to reduce the change in latent heating. Otherwise stated, the change in cloud radiative effects on the atmosphere reduces the change in the speed of the hydrologic cycle. If there were no changes in the cloud forcing, the hydrologic cycle at Pre-Industrial would be even faster relative to the Last Glacial Maximum.
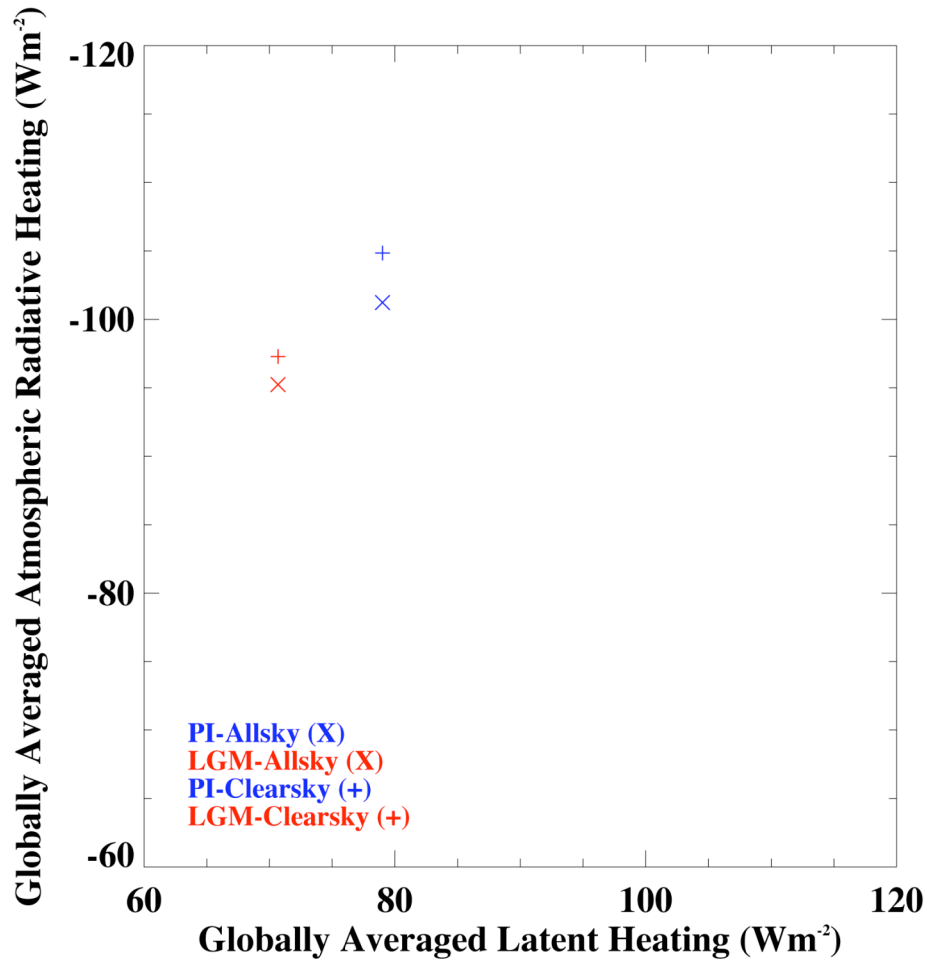
Figure 6.8: The atmospheric radiative cooling relationship with latent heating as computed from CCSM3 for Pre-industrial (blue) and Last Glacial Maximum (red).

6.4 Do the feedbacks amplify the climate change?

From what has been discussed in this chapter, the feedbacks act to amplify the climate change from Last Glacial Maximum to Pre-Industrial. Quantifying the feedbacks discussed in this chapter will show to what extent the climate feedbacks amplified the climate change from Last Glacial Maximum to Pre-Industrial. We choose to quantify the feedbacks in a simplified manner. For a more detailed look at quantifying feedbacks see Soden et al. (2008).

Table 6.1: Quantifying the cloud, ice-albedo, and water vapor feedbacks for the LGM, PI, and PI minus LGM in W m^{-2}. Feedback strength in W m^{-2} K^{-1} is shown in the far right column and was computed by taking the ratio of the feedback difference between PI and LGM and the Surface Temperature difference of 4.9 K.

	Radiative Feedbacks			
	LGM	PI	Feedback PI-LGM	Feedback Strength
Cloud				
Cloud forcing at surface	-81.94	-90.55	-8.61	-1.76
Ice-Albedo				
Clear-sky reflected SW at surface	-44.14	-32.46	11.68	2.38
Water Vapor				
Clear-sky downwelling LW at surface	274.76	299.45	24.69	5.04
		TOTAL	27.76 W m^{-2}	5.67 W m^{-2} K^{-1}

Table 6.1 shows the variables used to quantify the ice-albedo, water vapor, and cloud feedbacks at the surface, and the numerical value of each. It is evident, that the cloud feedback is negative and stronger cloud forcing occurs at Pre-Industrial, resulting in a -8.61 W m^{-2} change.

Throughout this chapter, the ice-albedo feedback has been considered a positive feedback. Table 6.1 indicates that the ice-albedo feedback is positive accounting for 11.68 W m^{-2} of the change. Globally averaged, sea ice area decreased from the transition between the LGM to PI climate indicating a positive feedback. In the Northern Hemisphere the amount of sea ice area increased in the since LGM due to a larger ocean basin at PI, allowing more sea ice to form. Changes in ocean basin size will be discussed later in this section.

The water vapor feedback is by far the largest feedback, accounting for most of the climate change by contributing 24.69 W m^{-2} to the total change. Combined, the radiative feedbacks represent a 27.76 W m^{-2} change. The last column of Table 6.1 indicates the feedback strength of the cloud, ice-albedo, and water vapor feedbacks.

Feedback strength is shown in the far right column, and was computed by taking the ratio of the feedback difference between PI and LGM and the surface temperature difference of 4.9 K. All together, from Last Glacial Maximum to Pre-Industrial, the feedbacks act to amplify the climate change by 5.67 W m^{-2} K^{-1}.

6.4.1   How does the ocean basin size affect the ice-albedo feedback?

Table 6.2 shows the Northern Hemisphere all-sky and clear-sky (CS) reflected shortwave radiation at the surface for the ocean only. The all-sky and clear-sky values are shown in Table 6.2 to reveal how the reflected shortwave changes with the presence of clouds. The Northern Hemisphere is shown since the sea ice in the Arctic Ocean persists through the change in climate from Last Glacial Maximum to Pre-Industrial. There is a decrease in the all-sky and clear-sky reflected shortwave at the surface during each season (i.e., annually and during the winter), except during the summer months of JJA where clear-sky reflected shortwave increases from LGM to PI by 0.11 W m^{-2}. This increase in clear-sky shortwave radiation is due to a 14% increase in ocean basin size. From Table 6.2, it can be seen that the change in ocean basin size drives the positive ice-albedo feedback. Changes in the Arctic ocean basin size can be seen in the North Pole stereographic map for the LGM (left) and PI (right) in Figure 6.9.

Figure 6.10 is the annual zonal mean clear-sky reflected shortwave radiation at the surface for the ocean only. Greatest changes in the clear-sky reflected shortwave at the surface are found in the high latitudes of both hemispheres. It is strongest at LGM in the Southern Hemisphere and most of the Northern Hemisphere. An exception to this is between the North Pole and 60º N, where the clear-sky reflected SW is greatest at PI.

This is because the Arctic Ocean has expanded in size since the LGM allowing for more reflection of shortwave radiation.

Table 6.2: Northern Hemisphere all-sky and clear-sky (CS) reflected shortwave radiation (SW) at the surface (ocean only) for LGM, PI, and PI minus LGM in W m^{-2}. The reflected shortwave radiation is also shown in Watts within the parentheses to include changes in ocean basin size. Table 6.2 is separated into Annual, June-July-August (JJA), and December-January-February (DJF).

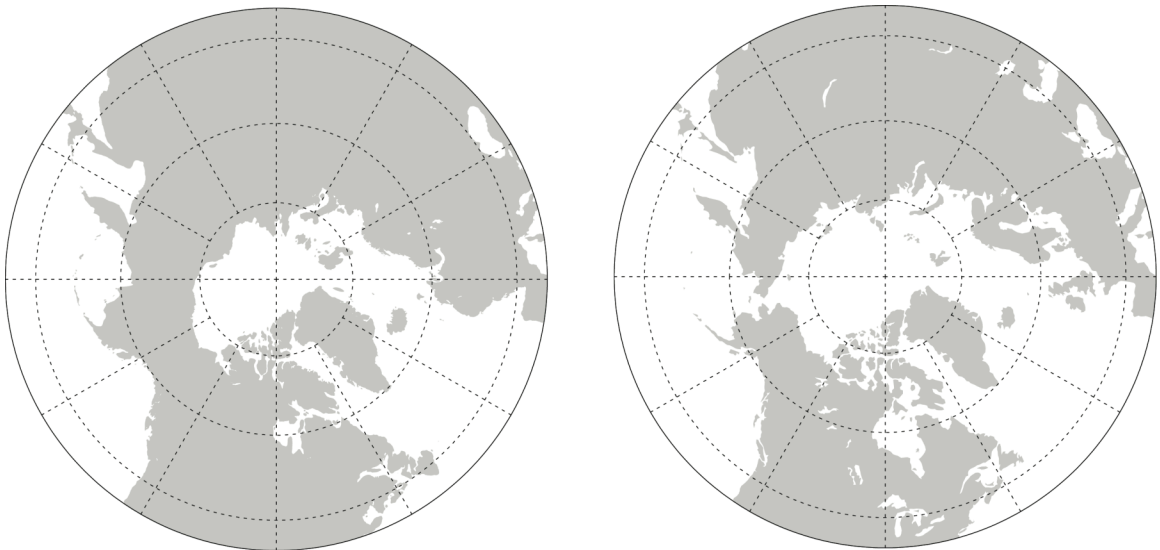| Northern Hemiphere Reflected Shortwave Radiation at the Surface		
LGM	PI	PI - LGM
Annual		
All-sky		
10.26 (9.16 E+14)	9.99 (1.00 E+15)	-0.27
Clear-sky		
13.20 (1.18 E+15)	13.13 (1.32 E+15)	-0.07
JJA		
All-sky		
10.53 (9.50 E+14)	10.30 (1.06 E+15)	-0.23
Clear-sky		
13.39 (1.21 E+15)	13.50 (1.38 E+15)	0.11
DJF		
All-sky		
9.59 (8.86 E+14)	9.23 (9.54 E+14)	-0.36
Clear-sky		
12.94 (1.19 E+15)	12.67 (1.31 E+15)	-0.27

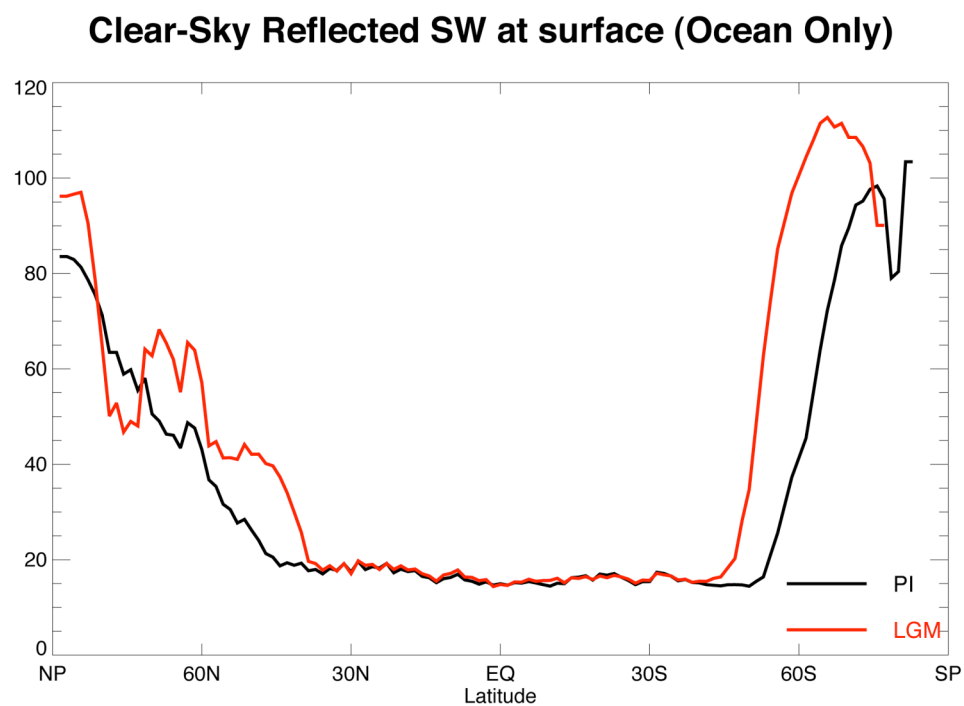Figure 6.9: North Pole stereographic map for the LGM (left) and PI (right).

Figure 6.10: Annual zonal mean clear-sky reflected shortwave radiation in W m^{-2} at the surface for the ocean only. Pre-Industrial is shown in black and the Last Glacial Maximum in red.

CHAPTER 7

Conclusions

In this study we compare the climates of the Last Glacial Maximum and Pre-Industrial simulated by the Community Climate System Model 3. Climate feedbacks that occur due to hydrological and energy cycle changes are the focus of this thesis. The Last Glacial Maximum (LGM), defined as the climate at 21 ka (21,000 years BP), was the peak of the last glacial period. During this period ice sheets in the Northern Hemisphere were at their greatest extent. The external forcings of the climate system between the glacial (i.e., LGM) and interglacial (i.e., PI) climates are significantly different and have a major impact on the mean climate. Reduced atmospheric trace gases, lowered sea level, and the presence of inland ice sheets in the Northern Hemisphere are some of the main differences between the two climates.

The LGM simulated climate is colder and drier than the PI climate. Global warming of 4.9 K is simulated at PI, with amplified warming in the high latitudes. Precipitation and evaporation increases of up to 2 mm day^{-1} exist where the continental ice sheets have melted away, with globally averaged increases of 0.33 mm day^{-1} from

LGM to PI. Precipitable water increases at PI by 20% compared to LGM. Combined increases in precipitation, evaporation, and precipitable water reflect a faster hydrological cycle at PI.

Changes in clouds lead to a stronger atmospheric radiative cooling effect at PI than LGM, and therefore promote increased precipitation. The change in radiative cooling from clear-sky to all-sky implies smaller changes in latent heating (i.e., the precipitation rate). In other words, if there were no differences in the cloud forcing, the hydrologic cycle at PI would be even faster relative to LGM.

The water vapor, ice-albedo, and cloud feedbacks act to amplify the climate change from LGM to PI. The positive water vapor and ice-albedo feedbacks account for 5.04 W m^{-2} K^{-1} and 2.38 W m^{-2} K^{-1}, respectively of the climate change. The cloud feedbacks produces -2.83 of the change. Refer to Table 6.1. An interesting and unexpected result was that the sign of the ice-albedo feedback changed regionally and is driven by changes in ocean basin size, particularly in the Arctic Ocean. Combined, the radiative feedbacks from LGM to PI act to amplify the climate change by 5.67 W m^{-2} K^{-1} and are balanced by an increase in surface evaporation.

7.1   Future work

For future work, it would be exciting to implement a dynamic ice sheet model, to allow the simulation of the deglaciation of the Northern Hemisphere. Incorporating dynamic vegetation into the Community Land Model component of the CCSM3 would help to determine the changes in surface albedo and other variables that affect the radiation budget, and allow the biogeochemical feedback to be included. Quantifying the climate feedbacks in this thesis was done in a simplified manner and a more thorough analysis and quantification of the feedbacks is needed to more fully determine how the

feedbacks amplified the climate change. It is our hope that this same analysis will be

carried out to compare the Last Glacial Maximum to future scenarios like those of the

IPCC AR4.

References

Blackmon, M. B., B. Boville, F. Bryan, R. Dickinson, P. Gent, J. Kiehl, R. Moritz, D. Randall, J. Shukla, S. Solomon, G. Bonan, S. Doney, I. Fung, J. Hack, E. Hunke, J. Hurrell, J. Kutzbach, J. Meehl, B. Otto-Bliesner, K. Taylor, J. Tribbia, and W. Washington, 2001: The community climate system model. *Bull. Amer. Meteor. Soc.*, **82,** 2357-2376**.**

Bony, S., R. Colman, V.M. Kattsov, R.P. Allan, C.S. Bretherton, J.-L. Dufresne, A. Hall, S. Hallegatte, M.M. Holland, W. Ingram, D.A. Randall, D.J. Soden, G. Tselioudis, and M.J. Webb, 2006: How well do we understand and evaluate climate change feedback processes? *J. Climate*, **19**, 3445-3482.

Braconnot, P., Otto-Bliesner, B., Harrison, S., Joussaume, S, Peterchmitt, J.-Y., Abe-Ouchi, A., Crucifix, M. , Driesschaert, E., Fichefet, Th., Hewitt, C. D., Kageyama, M., Kitoh, A., Laine, A., Loutre, M.-F., Marti, O., Merkel, U., Ramstein, G., Valdes, P., Weber, L. ,Yu, Y., and Zhao, Y., 2007: Results of PMIP2 coupled simulations of the mid-Holocene and Last Glacial Maximum - Part 1: experiments and large-scale features, *Clim. Past,* **3**, 261-277.

Bradley, R.S., 1999. *Paleoclimatology: Reconstructing Climates of the Quaternary.* Academic Press, San Diego, 610 pp.

Broccoli, A. J., 2000: Tropical cooling at the Last Glacial Maximum: An atmosphere-mixed layer ocean model simulation. *Journal of Climate*, **13**, 951-976.

Cai M., 2005: Dynamical amplification of polar warming, *Geophys. Res. Lett.*, 32, L22710, doi:10.1029/2005GL024481.

CLIMAP Project Members, 1981. Seasonal reconstruction of the earth's surface at the last glacial maximum. *Geol. Soc. Am. Map Chart Ser*. **MC-36**.

Collins, W.D., C.M. Bitz, M.L. Blackmon, G.B. Bonan, C.S. Bretherton, J.A. Carton, P. Chang, S.C. Doney, J.J. Hack, T.B. Henderson, J.T. Kiehl, W.G. Large, D.S. McKenna, B.D. Santer, and R.D. Smith, 2006: The community climate system model version 3 (CCSM3*). J. Climate*, **19**, 2122–2143.

Crowley, T.J., and G.R. North, 1991: *Paleoclimatology*. Oxford University Press, Oxford, 339 pp.

Fowler, L. D., and D. A. Randall, 1994: A global radiative-convective feedback. *Geophys. Res. Lett.*, **21**, 2035-2038.

Gates, W.L., 1976: The numerical simulation of ice-age climate with a global general circulation model. *J. Atmos. Sci.*, **33**, 1844–1873.

Hall, A., 2004: The role of surface albedo feedback in climate. *J. Climate*, **17**, 1550-1568.

Hartmann, D., 1994: *Global Physical Climatology*. Academic Press, 411pp.

Hewitt, C. D. and J. F. B. Mitchell (1997). Radiative forcing and response of a GCM to ice age boundary conditions: cloud feedback and climate sensitivity. *Climate Dynamics,* **13**, 821-834.

Holland, M.M. and C.M. Bitz, 2003: Polar amplification of climate change in the coupled model intercomparison project, Climate Dynamics, **21**, 221-232.

Hunke, E. C. and J. K. Dukowicz, 1997: An elastic-viscous-plastic model for sea ice dynamics, *J. Phys. Oceanogr.*, 27, 1849-1868.

Imbrie, J.L. and K.P. Imbrie, 1979. *Ice Ages: Solving the Mystery,* Harvard University Press, 224 pp.

Jansen, E., J. Overpeck, K.R. Briffa, J.-C. Duplessy, F. Joos, V. Masson-Delmotte, D. Olago, B. Otto-Bliesner, W.R. Peltier, S. Rahmstorf, R. Ramesh, D. Raynaud, D. Rind, O. Solomina, R. Villalba and D. Zhang, 2007: Palaeoclimate. In: *Climate Change 2007: The Physical Science Basis. Contribution of Working Group I to the Fourth Assessment Report of the Intergovernmental Panel on Climate Change* [Solomon, S., D. Qin, M. Manning, Z. Chen, M. Marquis, K.B. Averyt, M. Tignor and H.L. Miller (eds.)]. Cambridge University Press, Cambridge, United Kingdom and New York, NY, USA.

Kiehl, J. T., and P. R. Gent, 2004: The community climate system model, version two. *J. Clim*., **17**, 3666-3682**.**

Kiehl, J.T., C.A. Shields, J.J. Hack, and W.D. Collins, 2006: The Climate Sensitivity of the Community Climate System Model Version 3 (CCSM3). *J. Climate*, 19, 2584–2596.

Kutzbach, J.E., and H.E. Wright, Jr., 1985: Simulation of the climate of 18,000 yr BP: Results for the North American/North Atlantic/European Sector. *Quat. Sci. Rev.*, **4**, 147-187.

Manabe, S. and A.J. Broccoli, 1985: The influence of continental ice sheets on the climate of an ice age. *J. Geophys. Res.*, **90**, 2167-2190.

Manabe, S. and D.G. Hahn, 1977: Simulation of the tropical climate of an ice age. *J Geophys Res.,* **82**, 3889-3911.

Masson-Delmotte, V., Kageyama, M., Braconnot, P., Charbit, S., Krinner, G., Ritz, C., Guilyardi, E., Jouzel, J., Abe-Ouchi, A., Crucifix, M., Gladstone, R., Hewitt, C., Kitoh, A., LeGrande, A., Marti, O., Merkel, U., Motoi, T., Ohgaito, R., Otto-Bliesner, B., Peltier, W., Ross, I., Valdes, P., Vettoretti, G., Weber, S., Wolk, F., and Yu, Y., 2006: Past and future polar amplification of climate change: climate model intercomparisons and ice-core constraints, Clim. Dyn., 26, 513–529.

National Research Council, 2003. *Understanding Climate Change Feedbacks*. The National Academies Press, Washington, D.C., 166 pp.

Otto-Bliesner, B.L., E. Brady, G. Clauzet, R. Tomas, S. Levis, and Z. Kothavala, 2006a: Last glacial maximum and Holocene climate in CCSM3. *J. Climate*, **19**, 2526-2544.

Otto-Bliesner, B.L., R. Tomas, E.C. Brady, C. Ammann, Z. Kothavala, and G. Clauzet, 2006b: Climate sensitivity of moderate- and low-resolution versions of CCSM3 to preindustrial forcings. *J. Climate*, **19**, 2567–2583.

Peixoto, J.P. and A.H. Oort, 1992: *Physics of Climate*. American Institute of Physics, 520 pp.

Peltier, W.R., 2004: Global glacial isostasy and the surface of the ice-age Earth: the ICE-5G (VM2) model and GRACE. Annual Review of Earth and Planetary Sciences, **32**, 111-149.

PMIP, cited 2008: Paleoclimate Intercomparison Modeling Project. [Available online at http://pmip.lsce.ipsl.fr/].

PMIP 2, cited 2008: Paleoclimate Intercomparison Modeling Project Phase II. [Available online at http://pmip2.lsce.ipsl.fr/].

Ramaswamy, V., and Coauthors, 2001: Radiative forcing of climate change. Climate Change 2001: The Scientific Basis, J.T. Houghton et al., Eds., Cambridge University Press, 349-416.

Randall, D. A., Harshvardhan, D. A. Dazlich, and T. G. Corsetti, 1989: Interactions Among Radiation, Convection, and Large-Scale Dynamics in a General Circulation Model. *J. Atmos. Sci*., **46**, 1943-1970.

Shin S.-I., Z. Liu, B. L. Otto-Bliesner, J. E. Kutzbach, and S. J. Vavrus, 2003: Southern Ocean sea-ice control of the glacial North Atlantic thermohaline circulation, *Geophys. Res. Lett.*, **30** (2), 1096, doi:10.1029/2002GL015513.

Slingo, A., and J. M. Slingo, 1988: Response of a general circulation model to cloud long-wave radiative forcing. Part I: Introduction and initial experiments. *Quart. J. Roy. Meteor. Soc*., **114**, 1027–1062.

Stephens, G.L., 2005: Cloud Feedbacks in the Climate System: A Critical Review. *J. Climate,* **18**, 237–273.

Stephens, G.L., N. Slingo, M.J. Webb, P.J. Minnett, P.H. Daum, L. Kleiman, I. Wittmeyer, and D.A. Randall, 1994: Observations of the Earth's radiation budget in relation to atmospheric hydrology. Part IV: Atmospheric column radiative cooling over the worlds' oceans. *J. Geophys. Res*., **99**, 18585-18604.

Sugi, M., A. Noda, and N. Subo, 2002: Influence of the global warming of tropical cyclone climatology: An experiment with the JMA global model. *J. Meteor. Soc. Japan*, **80**, 249–272.

UCAR, cited 2008: Windows to the Universe. [Available online at

  http://www.windows.ucar.edu/].

Wallace, J.M. and P.V. Hobbs, 1977: *Atmospheric Science: An Introductory Survey*.

  Academic Press, 467 pp.

Wielicki, B. A., R. D. Cess, M. D. King, D. A. Randall, and E. F. Harrison, 1995:

  Mission to planet Earth: Role of clouds and radiation in climate. *Bull. Amer.*

  Meteor. Soc., **76,** 2125–2153.